


JES FOCUS ISSUE ON ELECTROCHEMICAL TECHNIQUES IN CORROSION SCIENCE IN MEMORY OF HUGH ISAACS
In Operando Analysis of Passive Film Growth on Ni-Cr and Ni-Cr-Mo Alloys in Chloride Solutions
Katie Lutton Cwalina,^{1,2,*} Hung M. Ha,³ Noemie Ott,⁴ Petra Reinke,² Nick Birbilis,^{4,} and John R. Scully^{1,2,**}**
¹Center for Electrochemical Science and Engineering, University of Virginia, Charlottesville, Virginia 22904, USA

²Department of Materials Science and Engineering, University of Virginia, Charlottesville, Virginia 22904, USA

³Canadian Nuclear Laboratories, Chalk River, Ontario K0J 1J0, Canada

⁴Department of Materials Science and Engineering, Monash University, Vic 3800, Australia

The instantaneous kinetics of oxide formation and growth, in competition with passive film dissolution and breakdown, were investigated for Ni-22 Cr and Ni-22 Cr-6 Mo (wt%) during single step passivation at +0.2 V_{SCE}. Experiments were conducted in selected acidic and alkaline chloride-containing environments using simultaneous AC and DC electrochemistry; including on-line Inductively Coupled Plasma-Mass Spectrometry (ICP-MS). In parallel experiments, in-situ neutron reflectometry (NR) and ex-situ X-ray photoelectron spectroscopy (XPS) were utilized to characterize the formation of surface oxide films as a function of time. The specific roles of pH and Mo during passivation and breakdown kinetics are highlighted, providing an insight into the fate of the elements which comprise the alloys, and their effects on passivation behavior. It was observed that early oxidation of both Ni and Cr-species occurred in acidic electrolyte. Preferential dissolution of Ni²⁺ at later times enabled gradual Cr³⁺ enrichment within the surface film. However, greater relative stability of NiO and Ni(OH)₂ was observed in the alkaline condition. Upon alloying Ni-Cr with Mo, Cr³⁺ became increasingly enriched in the surface film during anodic polarization. Oxides were interpreted to consist of non-stoichiometric solid solutions formed via solute capture.

© The Author(s) 2019. Published by ECS. This is an open access article distributed under the terms of the Creative Commons Attribution 4.0 License (CC BY, <http://creativecommons.org/licenses/by/4.0/>), which permits unrestricted reuse of the work in any medium, provided the original work is properly cited. [DOI: 10.1149/2.0261911jes]



Manuscript submitted March 1, 2019; revised manuscript received May 6, 2019. Published May 16, 2019. *This paper is part of the JES Focus Issue on Electrochemical Techniques in Corrosion Science in Memory of Hugh Isaacs.*

Passivation studies for metals in aqueous electrolytes often use in-situ and ex-situ techniques to characterize and measure surface film growth. Such methods include, but not limited to: electrochemical impedance spectroscopy (EIS),¹⁻³ X-ray photoelectron spectroscopy (XPS),³⁻⁶ ellipsometry (5-7),⁷⁻¹⁰ neutron reflectometry (NR),¹¹⁻¹⁴ and time-of-flight secondary ion mass spectrometry (ToF-SIMS).^{1,15,16} However, with the exception of ellipsometry, these methods do not commonly yield in-operando information on electrochemical oxidation and are often applied ex-situ for analysis of films post-growth. Historically, single step passivation studies on metals have involved single transition metal elements in unbuffered or buffered borate electrolytes of alkaline pH, in which passive hydroxylated oxides are thermodynamically stable in the solution and 100% efficiency is observed. Hence, it is assumed that direct cation ejection and chemical dissolution are negligible.^{7,17-22} Often for multi-element alloy passivation studies, the roles of individual elements are simplified and films may be assumed to contain stoichiometric oxides or hydroxides of single cations or spinels, leading to generalizations and assumptions for analysis of electrochemical data.²³⁻²⁵

Characterization techniques based on the coupling of an electrochemical flow cell and a downstream analytical technique enable accurate measurement of the partial elemental dissolution reaction rates during electrochemical passivation.^{23,24,26-28} Atomic emission spectroelectrochemistry (AESEC) has provided in-situ characterization of anodic dissolution of 304 stainless steel,²³ passivation of binary Fe-Cr alloys,²⁴ and transpassive dissolution of Ni-Cr-Mo alloys.²⁹ These spectroelectrochemical techniques were coupled with other surface-sensitive methods to investigate the influence of minor alloying elements and surface structures on the breakdown of thin films on an air-oxidized Fe-Cr-Mo-based glassy alloy.³⁰ However, such studies lacked an investigation into the time-dependent contributions of individual elements on passive film growth, as well as any real-time assessment of oxide formation rates or molecular identity.

Ni-Cr, and in particular Ni-Cr-Mo, alloys exhibit exemplary passivity over a wide range of oxidizing and reducing environments, potentials, pH values, and temperatures.^{3,16,31-39} For such alloys, a bi-layer film structure is often reported, consisting of stoichiometric oxides, in which Cr₂O₃ or Cr(OH)₃ films are present at the metal/film interface; and NiO or Ni(OH)₂ are prevalent at the outer film/electrolyte interface.^{5,34,40} Recent electron energy loss spectroscopy results upon electrochemically and air-oxidized Ni-Cr-Mo have indicated nearly identical enrichment of Ni²⁺ and Cr³⁺ at their corresponding interfaces, and non-stoichiometric rocksalt and corundum-structured oxides were detected despite the negligible equilibrium solubility between NiO and Cr₂O₃.⁴¹⁻⁴⁴ Other experiments concerning the dry oxidation of Ni-Cr at 700°C performed using in-situ TEM have suggested fast formation of a NiO layer, followed by the growth of a sub-surface Cr₂O₃ layer and eventually the emergence of large NiCr₂O₄ islands.^{45,46}

The enrichment of Moⁿ⁺ at the Ni- or Cr-rich film/electrolyte interface in particular has also been observed in previous literature,^{1,5,15,29,40,47-50} but both the local and overall concentrations of these cations in the film are insufficient for forming phase-separated MoO_x. For Ni-Cr-Mo, it was observed that Moⁿ⁺ cations became captured in the passive film at solute concentrations near that of the bulk alloy as a result of the rapid oxidation front velocity.⁵⁰ Transmission electron microscopy (TEM) characterization after in-situ air oxidation demonstrated that Mo dopants in the passive film⁵⁰ stabilized cation vacancies and inhibited Kirkendall void formation by encouraging the nucleation of corundum,⁴¹ consistent with the proposed role of Mo on inhibiting localized breakdown of the passive film.^{51,52}

The roles of minor alloying elements in Ni alloys have been previously studied using mainly ex-situ techniques.^{1,51,53,54} When Cr and Mo were alloyed together, synergistic passivity was observed.^{16,51,55} The enrichment of Cr³⁺ and Mo^{4,5,6+} in passive films has been previously established for commercial Ni-based alloys.⁵² Moreover, it has been found that upon adding Mo to the alloy, increasing the aqueous chloride concentration, and/or decreasing the pH, the concentration of Cr³⁺ increases within the passive film.^{16,52} Mo has been shown to promote Cr-film growth and chemical stability in both Fe-Cr and Ni-Cr systems, but the exact atomistic mechanism by which this effect

*Electrochemical Society Member.

**Electrochemical Society Fellow.

[†]E-mail: kml2re@virginia.edu

occurs and how it arrives in oxides is not understood.^{52,56} One reason for this uncertainty is a lack of understanding regarding the fate of Mo during passivation. Molybdenum has been reported to exist in passive films in two cation states and in stratified layers, as Mo^{4+} at the inner metal/film barrier layer and as hydrated Mo^{6+} at the film/electrolyte interface.^{1,5,32,57,58} It has additionally been proposed that Mo^{6+} replaces Cr^{3+} in passive films, reducing the flux of point defects responsible for film breakdown.^{51,59,60} An additional theory regarding the role of Mo for facilitating repassivation involves the segregation of MoO_4^{2-} and CrO_4^{2-} to the film/electrolyte interface, which generates a cation selective region that increases film stability in chloride-rich environments.^{61,62} The presence of Mo in corrosion resistant alloys has often been attributed to improvements in repassivation behavior, due to a speculated preferential enrichment at crevice surfaces via polymeric Mo-containing or molybdate species (i.e. MoO_4^{2-}) which inhibit anodic dissolution.^{29,52,63,64} Hence the fate of Mo in passive films deserves further inquiry.

For multi-element alloys, passivation is complicated by varying contributions of single element cations to film growth or dissolution throughout repassivation. Recently, the present authors discussed the novel coupling of single frequency electrochemical impedance spectroscopy (SF-EIS) with inductively coupled plasma-mass spectrometry (ICP-MS) for analysis of in-operando passive film growth on Ni-Cr alloys in an acidic sulfate solution.²⁵ The results demonstrated that significant cation dissolution occurs at all stages of nucleation and growth in acid solution (0.1 M Na_2SO_4 pH 5.5). Therefore, independent tracking of the oxidation contribution to electrochemically measured charge and anodic current density of each element in a multi-component alloy, along with the total anodic current density is necessary in order to improve the understanding of passivity.²⁵ Early formation of Ni-oxides or hydroxides was observed as they are more kinetically and epitaxially favored.^{25,65} Soon after, however, a Cr-rich film began to dominate due to selective Ni and Mo dissolution, whereupon a limiting film thickness was reached after 10 ks of passivation. At this point, the aqueous oxidation rate became equivalent to the rate of dissolution at the film/electrolyte interface.²⁵

The SF-EIS technique was later applied in conjunction with AFM measurements to characterize film growth and repassivation on single crystal Ni-Cr and Ni-Cr-Mo alloys exposed to an acidified chloride solution.⁶⁶ The results demonstrated the passivation on grain surfaces which were oriented near (1 0 1) for Ni-11 Cr (wt%), whereas those containing 6 wt% Mo exhibited stable, conformal, passive films for every orientation probed. The existence of a matchstick-type morphology of the etched, unoxidized (1 0 1) surfaces suggested that the improved film stability was a result of favorable oxide epitaxy along the nanofacets, whereas Mo enabled repassivation along surfaces of various orientations and topographies. Notably, the application of SF-EIS in this previous study enabled the extraction of the film thickness, $l_{\text{ox}}(t)$, and the total oxidation rate, $i_{\text{ox}}(t)$, on individual grains. From this information, the Cabrera-Mott model for high field film growth^{17,67} was applied to successfully compute the relevant kinetic parameters and enable a comparison between the different grain orientations. Despite all this work, an in-operando study of such multi-component alloys tracking the fate of each element is lacking for Ni-Cr alloys except for a recent study limited to the transpassive potential range and subsequent repassivation.²⁹

This paper discusses the utilization of complementary and in-operando ICP-MS and SF-EIS for polycrystalline Ni-22 Cr and Ni-22 Cr-6 Mo, wt%, and, on a set of model alloys, in-situ NR in chloride environments. This approach enables tracking of each element and overcomes many of the assumptions used in previous passivity studies. In particular, extraction of the oxidation contribution from the total anodic current density for each alloying element enables a more

^aAccording to the Solute Vacancy Interaction Model (SVIM), minor alloying elements such as Mo and W inhibit film breakdown by forming positively charged substitutional dopants which electrostatically attract detrimental, negatively charged cation vacancies and inhibit their motion.⁵¹ Cation vacancies are theorized to coalesce into Kirkendall voids at the metal/film interface and eventually initiate breakdown.^{41,60}

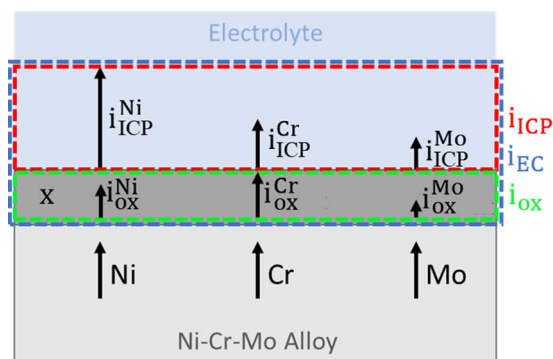


Figure 1. Schematic of the dissolution and oxidation reactions occurring for a Ni-Cr-Mo alloy with the corresponding current densities indicated.

accurate measurement of passivation in aqueous solutions where dissolution can be significant. It is shown that oxidation efficiency varies with alloy composition and electrolyte pH. The combination of in-operando techniques enables an improved understanding of the role and fate of minor alloying elements such as Mo during aqueous passive film growth and dissolution in acidic and alkaline chloride environments. The results are consistent with previous observations that Mo^{4+} and Mo^{6+} are solute captured in a non-stoichiometric oxide.⁵⁰ In-situ NR and ex-situ XPS validated the evolution of film composition determined using ICP-MS plus SF-EIS and identified the chemical species present in the oxide. These approaches can be extended to other alloy systems such as metallic glasses or multi-principal-element, high-entropy alloys where multi-element passivation must be considered.^{28,68}

Materials and Experimental Procedure

The samples used for ICP-MS and SF-EIS were polycrystalline, solid solution Ni-alloys that modelled common Cr and Mo concentrations found in commercial Ni-superalloys with the following compositions: Ni-22 Cr and Ni-22 Cr-6 Mo, wt%. The materials were arc-melted, cast, rolled, solutionized, recrystallized, and sectioned. Prior to each experiment, the samples were abraded up to 1200 grit using SiC paper, ultrasonically cleaned in alcohol, and rinsed with deionized water (resistivity of 18.2 $\text{M}\Omega\text{-cm}$) before being placed into the flat cell window.

For the purpose of the NR experiments, thin films were prepared by a sputter deposition system (Plasmionique Inc., Quebec, Canada) to produce approximate 25 nm thick Ni-Cr and Ni-Cr-Mo alloys with a surface roughness of 5 \AA on 100 mm diameter \times 6 mm thick polished Si(111) wafers. XPS analysis following thin film preparation yielded alloy compositions of Ni-20 Cr and Ni-20 Cr-10 Mo, wt%. The solutions used were 0.1 M NaCl pH, adjusted to pH 4 and 10 using 1 M HCl and 1 M NaOH, respectively. All prepared solutions used reagent grade chemicals dissolved in deionized water dispensed from a Milli-Q system and were deaerated using ultra-high purity N_2 gas during electrochemical experimentation.

Electrochemical control was maintained using a Bio-Logic SP-150 potentiostat. Initial cathodic polarization at $-1.3 V_{\text{SCE}}$ was performed for 10 min to minimize air-formed oxides.^{3,69} Following this, a potentiostatic step to $+0.2 V_{\text{SCE}}$ was implemented to grow the oxide within the passive region for time periods up to 10 ks. In-operando ICP-MS experiments were carried out for this 10 ks period using an experimental setup that has been detailed previously, along with the relevant limits of detection: $2.70 \pm 0.30 \mu\text{g/L}$ for Cr,⁵⁰ $0.27 \pm 0.12 \mu\text{g/L}$ for Ni⁵⁸ and $0.074 \pm 0.013 \mu\text{g/L}$ for Mo.^{25,98} Therefore, the corresponding current density detection limits are approximately $7.0 \times 10^{-7} \text{ A/cm}^2$ for Cr^{3+} , $4.1 \times 10^{-8} \text{ A/cm}^2$ for Ni^{2+} , and $2.1 \times 10^{-8} \text{ A/cm}^2$ for Mo^{6+} (Eq. A1). Only concentration data above the detection limits were considered. A general schematic of the relative oxidation and dissolution rates for individual alloying elements is given in Figure 1. The

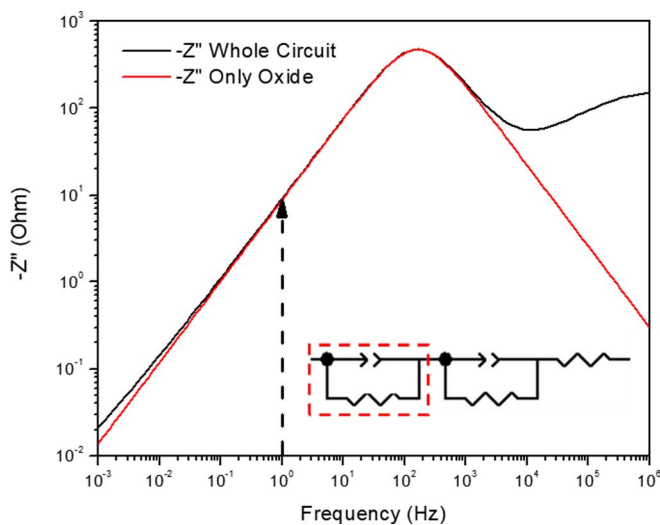


Figure 2. Comparison of the total $-Z''$ spectra of Ni-22 Cr-6 Mo, wt%, after 10 ks of potentiostatic polarization at $+0.2 V_{SCE}$ in 0.1 M NaCl pH 4 versus a ZView simulation using a simplified circuit fit containing only a constant phase element and a resistor with the same measured Q_{CPE} , α , and R_{ox} from fitting the total spectra, as indicated in the inset model where the red outline indicates the oxide portion, demonstrating that using $-Z''$ at 1 Hz correlates to the oxide properties.

ICP-MS results and i_{EC} were analyzed according to previously established procedures^{23,25} presented in Appendix A to arrive at the differences in the net dissolution and oxidation of individual elements. The instantaneous electrochemical signals were convoluted onto the same time scale as ICP-MS measurements.

The electrochemical cell for the SF-EIS experiments was a typical three-electrode flat cell with a Pt mesh counter electrode and a mercury-mercury sulfate reference electrode (MMSE, $+0.41 V_{SCE}$). The still solution was identically deaerated and the initial cathodic reduction step was also utilized to partially reduce any air-formed oxide.^{3,69} For the SF-EIS measurements, a Gamry Reference 600 potentiostat was used. The Gamry SF-EIS script was applied at $+0.2 V_{SCE}$ with a frequency of 1 Hz and an AC amplitude of 20 mV during potentiostatic film growth over 10 ks. Following SF-EIS, an EIS spectrum was acquired at the same potential, $+0.2 V_{SCE}$, from 100 kHz to 1 MHz for rigorous correlation of the imaginary impedance data (Z'') to an oxide thickness using an electrical equivalent circuit model developed for Ni-Cr alloys.³ The exact method has been previously introduced²⁵ and is discussed in more detail in Appendix B.

For application of this technique, the frequency of 1 Hz was chosen to provide relatively fast impedance measurements which were still representative of the oxide layer, rather than other interfacial or solution processes. This was confirmed by measuring a full EIS spectrum at frequencies ranging from 100 kHz to 1 mHz as shown in Figure 2 and fitting the aforementioned electrical equivalent circuit model to the data.³ The oxide was modeled as a constant phase element and resistor in parallel and the fitted Q_{CPE} , α , and R_{ox} were inputted into a ZView simulation of the series circuit model. The simulated $-Z''$ at varying frequencies is given in Figure 2 and compared to the full spectrum. It can be verified that the impedance measured at the chosen frequency is dominated by the CPE associated with the oxide layer rather than the interface or solution. A wide range of frequencies can be used, but 1 Hz was chosen to simplify the application of Eq. B4.

Following electrochemical testing, samples were cleaned with deionized water and sonicated in ethanol before being dried and transported using a container filled with Ar gas. All XPS spectra were obtained using a monochromatic Al- K_{α} photon source ($h\nu = 1,486.7$ eV). The angle between the sample and detector was fixed at 90° and that between detector and the X-ray source was 54.7° relative to the sample. Spectra were calibrated to the $4f^{7/2}$ binding energy of a metallic Au

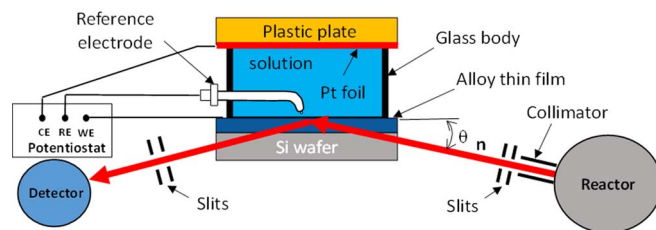


Figure 3. Schematic of the in-situ NR experiment at the D3 beamline of the NRU reactor.

reference (B.E. = 84 eV). Survey spectra were recorded on all samples using a pass energy of 200 eV, followed by focused spectra on the Ni 2p, Cr 2p, Mo 3d, and O 1s regions using a pass energy of 20 eV. Commercial CasaXPS software was used to perform Shirley background corrections and spectra fitting.⁷⁰⁻⁷² The concentrations of Ni^{2+} , Cr^{3+} , Mo^{4+} , and Mo^{6+} cations in the passive films were computed by fitting metallic and oxide/hydroxide peak positions and shapes established in previous literature to the experimental results,^{1,16,72-75} and correcting these integrated peak areas to atomic sensitivity factors for Ni, Cr, and Mo (4.044, 2.427, and 3.321 for this detector and source configuration, respectively).⁷²

The thin film samples prepared for NR were stored in a vacuum desiccator and, prior to experiments, were cleaned with methanol and dried in air. Figure 3 shows a schematic of the in-situ NR experimental setup at the D3 beamline at the National Research Universal (NRU) reactor (Chalk River, Ontario, Canada). This setup allowed NR measurements to be performed concurrently with electrochemical experiments. A conventional three-electrode electrochemical cell with a Pt thin foil counter electrode and a KCl saturated Ag/AgCl reference electrode ($V_{Ag/AgCl} = +47$ mV_{SCE}) was used. A Solartron 1287A potentiostat and a Solartron 1255 frequency analyzer were used in electrochemical experiments. A cathodic potential of $-1.2 V_{SCE}$ was applied for 5 min to minimize the air-formed oxide, followed by steps from $-0.8 V_{SCE}$ up to $+0.2 V_{SCE}$ in 0.2 V steps every 6 hr. The thin film samples, Pt foil, and reference electrode were connected to the corresponding terminals of the potentiostat for potential control and electrochemical measurements and the neutron beam travelled through the sample to the electrolyte, first reaching the Si layer as suggested in Figure 3. The NR measurements started 1 hr after the applied potential was switched to the set value and each measurement took approximately 90 min to complete.

D3 uses a collimated neutron beam with a wavelength of 2.37 \AA . The intensity of the specular reflected beam was recorded at different grazing angles, θ , and the reflectivity curves were plotted as a function of the scattering vector, Q , whose magnitude is related to the incident beam angle and the neutron wavelength by the following expression:^{76,77}

$$|Q| = \frac{4\pi}{\lambda} \sin \theta \#$$

The thickness, roughness, and neutron scattering length density (SLD) profile of the layers in the thin film sample were obtained by fitting the reflectivity curves to a thin film model using a least squares fit algorithm which includes a recursion algorithm developed by Parratt.⁷⁶⁻⁷⁹ The SLD is characteristic for a given molecule because of its proportionality to the intrinsic scattering length and density of atoms in the chemical formula unit. Therefore, modelling the SLD as a function of depth enables the distribution of molecular compounds with known densities to be characterized.¹¹

Results

Initial electrochemical characterization.—The E-log i passivation behavior of Ni-22 Cr and Ni-22 Cr-6 Mo, wt%, in the acidic and alkaline solutions was established initially (Figure 4a). The impedance was then measured at 1 Hz to assess the imaginary component of the isolated oxide film impedance and its corresponding capacitance

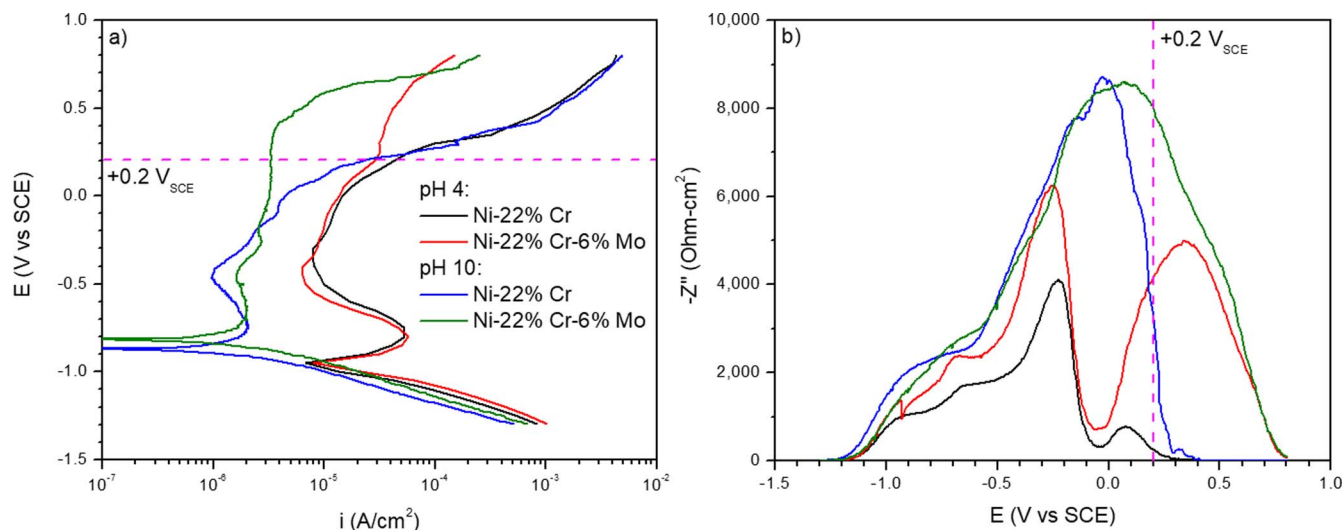


Figure 4. a) Current density and b) impedance variations during upward potentiodynamic polarization of Ni-22 Cr and Ni-22 Cr-6 Mo, wt%, in deaerated 0.1 M NaCl at pH 4 and 10 with the potential used in this study (+0.2 V_{SCE}) indicated.

across the same range of applied potentials during a potentiodynamic sweep from $-1.3 V_{SCE}$ to $+0.8 V_{SCE}$ at 1 mV/s (Figure 4b). The polarization behavior in Figure 4a shows a difference between the pH 4 and 10 environments with a lower passive current density in the latter environment. At $+0.2 V_{SCE}$, there is a clear difference in the impedance of passive films on Ni-Cr and Ni-Cr-Mo in both solutions and as such, this potential was selected for the potentiostatic experiments that will be discussed in detail herein. Specifically, this potential is also near the potential at which crevice corrosion occurs in seawater.^{64,80} This potential is thus of great technological relevance. The applied anodic potential, $+0.2 V_{SCE}$, is within the passive window of Ni-Cr-Mo in both solutions, and just at the potential above which the passive film degrades for Ni-Cr (Figure 4a). In Figure 4b, $-Z''$ rises at potentials above $-1.2 V_{SCE}$ and peaks at approximately $0 V_{SCE}$ for Ni-Cr films in pH 4 and the films on both alloys in the pH 10 environment, beginning to drop discernably above $+0.1 V_{SCE}$. Both the E-log i and impedance behavior are improved above $+0.2 V_{SCE}$ for Ni-Cr-Mo relative to Ni-Cr. Transpassivity in the acidic environment was shifted to potentials above $+0.4 V_{SCE}$ due to Mo stabilizing the passive film as observed elsewhere.^{29,49} $-Z''$ was near a maximum around $+0.2 V_{SCE}$ for Ni-Cr-Mo films in both solutions, whereas the impedance was already declining with increasing potential for Ni-Cr films due to chemical thinning and dissolution (Figure 4b).

In-Operando electrochemical passivation in 0.1 M NaCl pH 4.—

The element-specific dissolution current densities, i_{ICP}^M , for Ni-Cr and Ni-Cr-Mo and their passive films were measured along with the total electrochemical current density, i_{EC} . Using the latter current density, the rate of congruent dissolution for each element in the bulk alloy could be inferred (e.g. $i_{cong\ diss}^M = (at\% M)i_{EC}$)^b. The difference between i_{ICP}^M and $i_{cong\ diss}^M$ for each element, M, indicates the specific contribution toward direct film growth rather than cation ejection by direct oxidation or subsequent chemical dissolution of oxides initially formed.

In Figure 5a, i_{EC} , i_{ICP}^{Ni} , and i_{ICP}^{Cr} are smooth and decreasing during the first 300 s for the Ni-Cr alloy. i_{ox}^{Ni} and i_{ox}^{Cr} are similarly decreasing and remain in proportion to the alloy composition. Overall, the Cr-rich passive film is still thickening ($i_{cong\ diss}^{Cr} > i_{ICP}^{Cr}$) until ~ 400 s when i_{EC} , i_{ICP}^{Ni} , and i_{ICP}^{Cr} all increase as crevice corrosion initiates. Noticeably, from 100 to 400 s, i_{ICP}^{Cr} is below the aforementioned detection limit for Cr and as such, Cr is contributing toward film growth rather than

^bCongruent dissolution is a reasonable assumption when the kinetics for dissolution are faster than those for passivation, i.e. $i_{ICP} > i_{ox}$.

dissolution, whereas there is some Ni dissolution detected during the first 400 s. After approximately 1 ks, i_{ICP}^{Ni} and i_{ICP}^{Cr} approach their respective electrochemically derived currents for congruent dissolution during crevice corrosion attack which dominates the ICP-MS measurements from this time onward. There is some detected Cr dissolution on Ni-Cr (Figure 5a) at early times as i_{ICP}^{Cr} was above its corresponding detection limit (7.0×10^{-7} A/cm² for Cr³⁺).

The overall film formation rates for Ni-Cr (Eqs. A1–A7 and Figure 5a) according to the ICP-MS results were compared to those found using the SF-EIS in-operando technique (Eq. B4 and Figure 5b). For both techniques, i_{EC} , i_{ox} , and i_{ICP} initially decreased while i_{ox} increased at a decreasing rate overall before localized corrosion initiated. At this point, $i_{ox} \rightarrow 0$ as both i_{EC} and i_{ICP} increased. After crevice corrosion occurs, Eq. B2 is invalidated because localized attack dominates the impedance of the system, such that any measured Z'' reflected corrosion variations instead of film growth characteristics. Eqs. A4 and A6 are similarly nullified following localized corrosion, as an additional current density proportional to the crevice corrosion rate does not contribute to oxide formation. As such, the i_{ox} obtained using SF-EIS and ICP-MS results following crevice corrosion initiation were excluded from Figure 5b.

There is a noticeable distinction between the behaviors of the alloys in 0.1 M NaCl at pH 4: Ni-Cr exhibited crevice corrosion after approximately 300 s (Figure 5a) while Ni-Cr-Mo remained passive at all times (Figure 6a). All three alloying elements in Ni-Cr-Mo contributed to film formation, as evidenced by $i_{cong\ diss}^M > i_{ICP}^M$ until a steady-state thickness was approached at approximately 5 ks, indicated by the quasi-steady state level of i_{EC} . In particular, i_{ICP}^{Cr} and i_{ICP}^{Mo} were below the relevant detection limits from 400 to 10,000 s and less than $i_{cong\ diss}^M$, indicating that these elements joined the film, whereas selective dissolution of Ni occurred during film growth to compensate for the enrichment of the other metal cations. Because $i_{ICP}^{Ni} < i_{cong\ diss}^{Ni}$ up until 3 ks, there was still some net oxidation of Ni cations joining the passive film despite the simultaneous observation of dissolved species in the electrolyte stream.

Figure 6b shows a comparison between the ICP-MS and SF-EIS film growth calculations in the case of Ni-Cr-Mo. Unlike the results shown in Figure 5b, Ni-Cr-Mo remained passive with no crevice corrosion initiation throughout the experiment time as i_{EC} , i_{ICP} , and i_{ox} all decrease as i_{ox} increases and thus the two sets of film growth agree well with each other over the entire 10 ks. Overall, Ni-Cr exhibited a greater film growth rate and a noticeably higher i_{EC} than Ni-Cr-Mo (Figure 5). The improved passivity of Ni-Cr-Mo (Figure 6) clearly demonstrates one of the many proposed roles of Mo minor alloying additions⁵² related to increasing the electrochemical stability of the

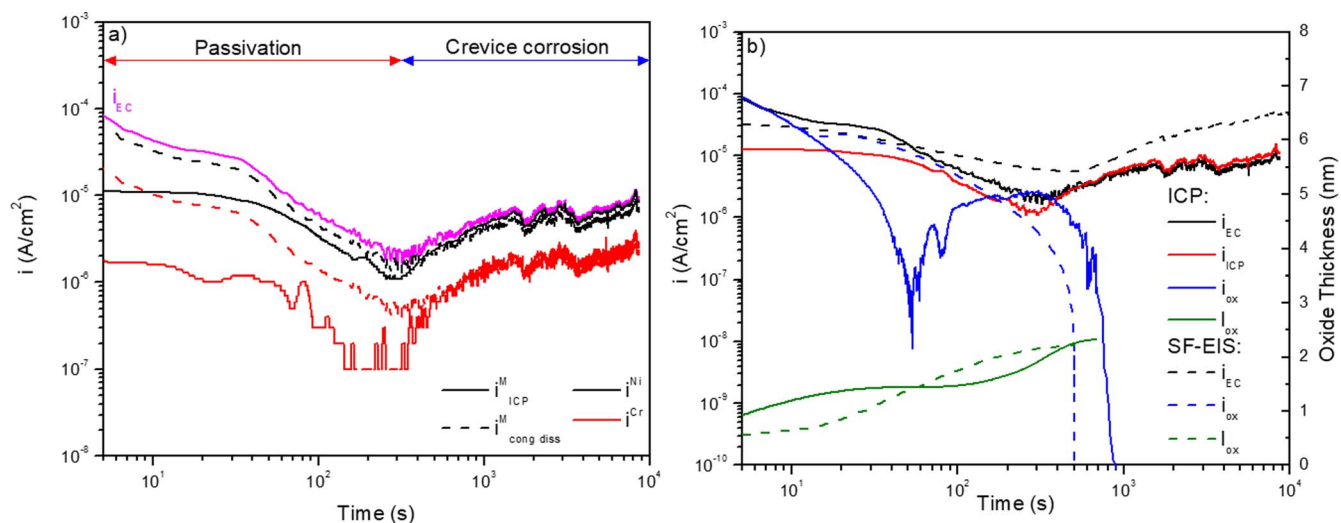


Figure 5. a) Calculated ICP-MS current densities for cation emission or dissolution versus the total element-specific current densities assuming congruent dissolution and b) ICP-MS and SF-EIS overall (i_{EC}), total dissolution (i_{ICP}), and oxidation (i_{ox}) current densities along with calculated film growth (l_{ox}) during passivation of Ni-22Cr at $+0.2 V_{SCE}$ in 0.1 M NaCl pH 4. Instantaneous DC currents had their time convoluted in order to place them on the same scale as ICP-MS measurements.

passive film. Both alloys reached similar maximum film thicknesses: approximately 2.1 nm for Ni-Cr before crevice corrosion initiated and 2.3 nm for Ni-Cr-Mo at the end of the passivation time. For Ni-Cr-Mo, l_{ox} levels off after 2–3 ks when i_{ICP} approaches i_{EC} suggesting any oxidation, i_{ox} , helps to maintain the passive film at more or less constant thickness (Figure 6).

The application of Eqs. A8 and A9 to the data shown in Figures 5a and 6a enabled computation of the film cation fraction during the passivation step (Figure 7). Both alloys become increasingly Cr-rich with time as Ni preferentially dissolves in the chloride-containing solution. The results indicate that the passive film on Ni-Cr-Mo is slightly more enriched with Cr cations compared to that observed on Ni-Cr over the first 10 ks, supporting an additional role of Mo as a promoter of preferential Cr-oxidation.⁵² Mo appears to be present only at small concentrations, reaching a maximum of 2.7% of all cations in the passive film by the end of the experiment. This small amount of Mo cations is unlikely to result in a distinct, stoichiometric MoO_x phase especially as a complete layer which would be less than one rutile unit cell thick unless it is present as small isolate islands (Figure 6a).

In-Operando electrochemical passivation in 0.1 M NaCl pH 10.

Potentiostatic passivation of Ni-Cr and Ni-Cr-Mo at $+0.2 V_{SCE}$ was also investigated in 0.1 M NaCl adjusted to pH 10 and monitored using SF-EIS and ICP-MS. The formation of kinetically favorable of oxide species vs. thermodynamic expected oxide was examined in alkaline environments, as previously outlined by Pourbaix.⁸¹ The dissolution current densities for specific alloying elements in Ni-Cr are indicated with a comparison to the total current density for electrochemical reactions during passivation. Substantial Ni and Cr oxidation occurs in the case of both alloys at all times ($i_{cong\ diss}^{Ni} > i_{ICP}^{Ni}$ and $i_{cong\ diss}^{Cr} > i_{ICP}^{Cr}$ at all times in Figure 8a).

The Ni-Cr film undergoes increased dissolution as i_{ICP}^{Ni} and i_{ICP}^{Cr} both begin to increase after 300 s (Figure 8a). It is observed that i_{ox}^{Ni} and i_{ox}^{Cr} remain high but there are “sharp” upward spikes of Ni and Cr dissolution where i_{ICP}^{Ni} and i_{ICP}^{Cr} increase and afterwards return to an approximately steady value. The film is experiencing periodic localized corrosion, rather than the stable crevice corrosion evidenced by the monotonically increasing i_{ICP} seen for pH 4 (Figure 5). It is worth noting that these peaks only appear sharp due to the logarithmic time scale, but they exhibit a residence time distribution characteris-

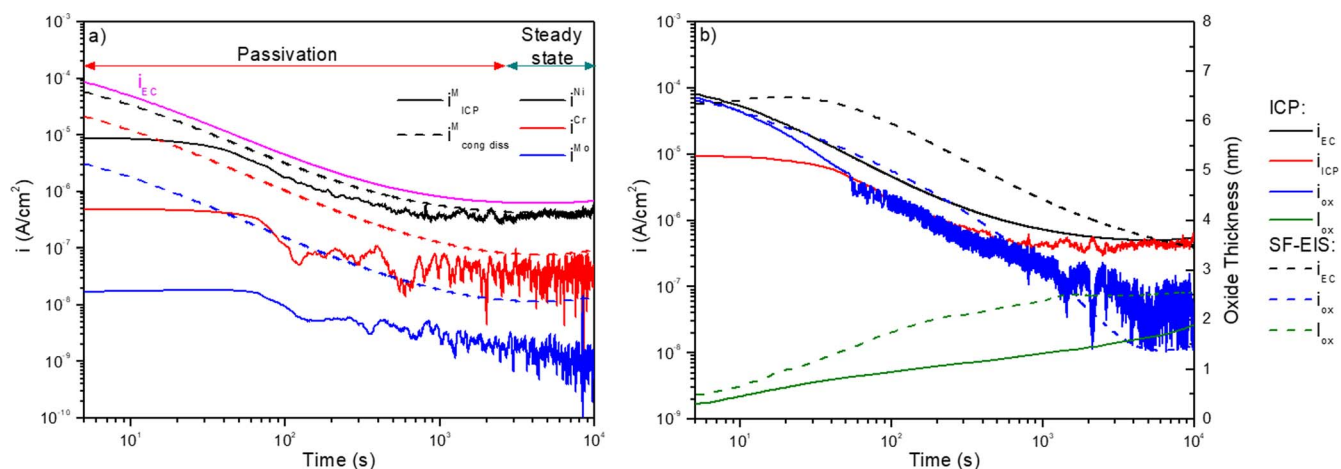


Figure 6. a) Calculated ICP-MS current densities for cation emission or dissolution versus the total element-specific current densities assuming congruent dissolution and b) ICP-MS and SF-EIS derived and overall (i_{EC}), total dissolution (i_{ICP}), and oxidation (i_{ox}) current densities along with calculated film growth (l_{ox}) during passivation of Ni-22Cr-6Mo at $+0.2 V_{SCE}$ in 0.1 M NaCl pH 4. Instantaneous DC currents densities had their time convoluted in order to place them on the same scale as ICP-MS measurements.

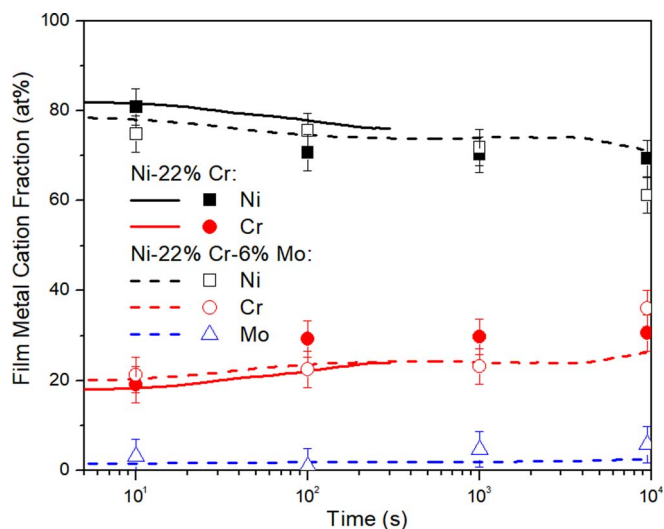


Figure 7. Relative accumulation of metal cations in the passive films during oxide growth until the time of localized corrosion initiation at $+0.2 V_{SCE}$ according to ICP-MS (lines) and XPS (symbols) measurements on Ni-22 Cr and Ni-22 Cr-6 Mo, wt%, in 0.1 M NaCl pH 4.

tic for flow cell-based measurements when plotted with a linear time axis.⁸² Spikes in i_{EC} for individual localized breakdown events could not be detected due to the low data acquisition rates. Instead, i_{EC} is smoother than i_{ICP} but exhibits abrupt spikes due to data sampling of parts of a breakdown event. As was observed in the pH 4 environments, good agreement regarding oxide thickness was obtained between the ICP-MS and SF-EIS techniques (Figure 8b). There is one difference, however, because the periodic and relatively infrequent occurrence of localized corrosion events did not significantly impact the impedance measurements. As such SF-EIS was a valid approach to determine oxide thickness during the entire 10 ks. Some fluctuations in Z'' were measured, evident in i_{ox}^{SF} (Figure 8b).

It is revealed that Ni-Cr-Mo has similar Ni and Cr oxidation behaviors at all times in the pH 10 environment (Figure 9a). The calculated i_{ox}^{Ni} appears to dominate film growth ($i_{cong diss}^{Ni} \gg i_{ICP}^{Ni}$) and the ICP-MS signal remains above the detection limit. As such, there is still some discernible dissolution, albeit less than was observed for Ni-Cr in either environment or Ni-Cr-Mo in pH 4 (Figure 6a), despite the more significant amounts of oxidation. This agrees with the predicted

Table I. Averaged oxidation efficiency (%) computed for the results shown in Figures 5–10 for Ni-22 Cr and Ni-22 Cr-6 Mo, wt%, passivated at $+0.2 V_{SCE}$ in 0.1 M NaCl for 10 ks with the pH adjusted to either 4 or 10.

Electrolyte	Ni-22 Cr	Ni-22 Cr-6 Mo
pH 4	4.0	31.5
pH 10	43.2	90.2

thermodynamic stability of NiO and Ni(OH)₂ at $+0.2 V_{SCE}$ in pH 10 environments.^{81,83,84} Concerning Ni-Cr-Mo alloys, the characteristic indications of localized corrosion were not observed using ICP-MS data, owing to the alloying with Mo. Additionally, Ni-Cr-Mo oxide films attain a nearly quasi-steady state overall thickness after 10 ks at pH 10 and do not indicate localized breakdown (Figure 9a). The very slight increase in i_{EC} after long times is, instead, caused by preferential dissolution of Mo from the passive film, as is evident in Figure 9a in which $i_{ICP}^{Mo} > i_{cong diss}^{Mo}$ after 1 ks. Mo-oxides are not predicted to be thermodynamically favorable in the alkaline environment; instead, soluble MoO_4^{2-} is expected.⁸¹

A comparison between the passivation kinetics measured using ICP-MS (Eq. A7) and SF-EIS (Eq. B4) for Ni-Cr-Mo in pH 10 NaCl are presented in Figure 9b. The methods predict similar trends, as discussed for the previous cases. The measured i_{ICP} is much higher for all times for Ni-Cr alloy compared to the Ni-Cr-Mo alloy due to the influence of Mo on facilitating passivation and resisting localized breakdown. The efficiency of film growth on Ni-Cr-Mo appears very high over all times ($i_{ox}^{ICP} \approx i_{EC}$ in Eq. A4). A major distinction between the alkaline experiments in Figures 8b and 9b and the acidic test in Figures 5b and 6b is the increased film growth in the latter; both alloys reached final thicknesses ranging from 5 to 7 nm in 0.1 M NaCl pH 10, greater than the 2 nm thickness in pH 4. The average electrochemical current efficiencies ($\eta = i_{ox}/i_{EC}$) were computed for each alloy and environment and are given in Table I. There is a significant difference between each alloy and environment. Ni-Cr had a much higher computed oxidation efficiency throughout the 10 ks potential step in the alkaline environment than in the acidic case. Notably, the high Ni-Cr efficiency in alkaline environments was slightly greater than that for Ni-Cr-Mo in the pH 4 environment due to the increased stability of Ni- and Cr-films. Ni-Cr-Mo had the greatest average efficiency in the pH 10 environment despite the significant selective dissolution of Mo at long times.

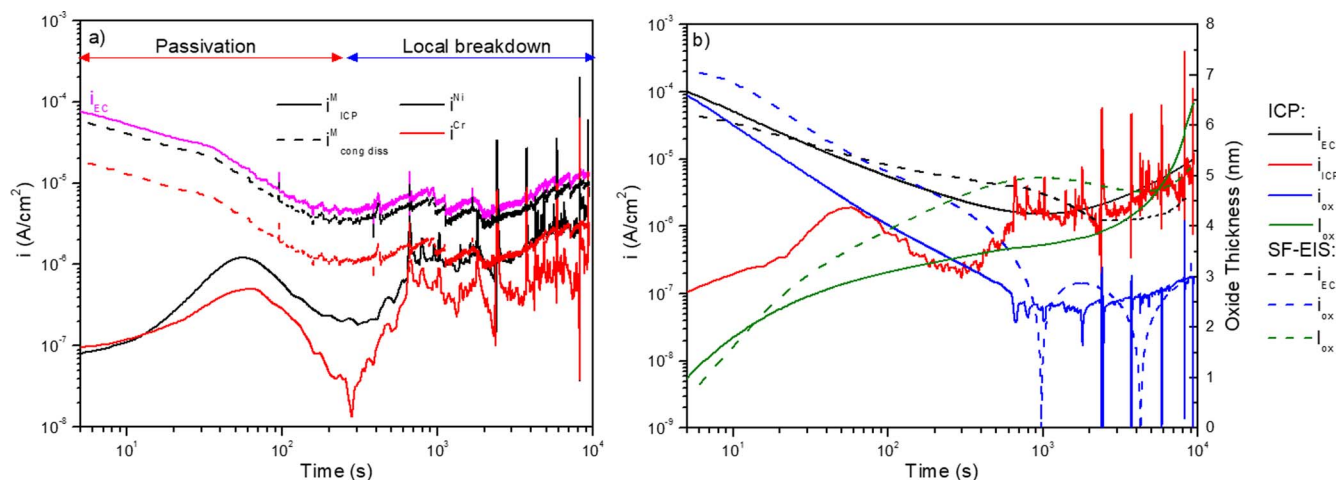


Figure 8. a) Calculated ICP-MS current densities for cation emission or dissolution versus the total element-specific current densities assuming congruent dissolution and b) ICP-MS and SF-EIS overall (i_{EC}), total dissolution (i_{ICP}), and oxidation (i_{ox}) current densities along with calculated film growth (i_{ox}) during passivation of Ni-22 Cr at $+0.2 V_{SCE}$ in 0.1 M NaCl pH 10. Instantaneous DC current densities had their time convoluted in order to put them on the same scale as ICP-MS measurements.

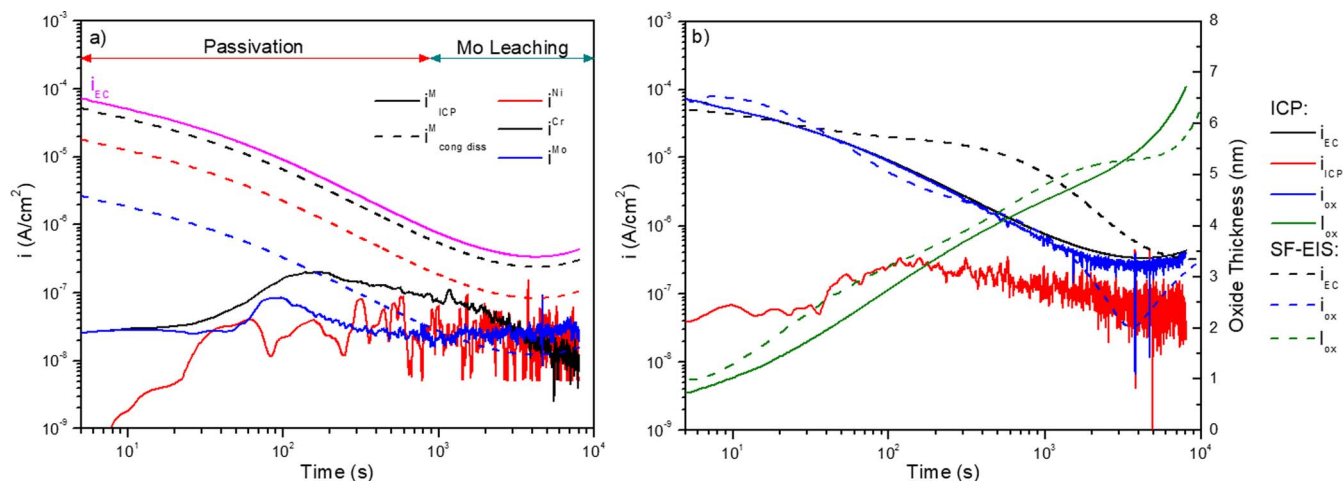


Figure 9. a) Calculated ICP-MS current densities for cation emission or dissolution versus the total element-specific current densities assuming congruent dissolution and b) ICP-MS and SF-EIS overall (i_{EC}), total dissolution (i_{ICP}), and oxidation (i_{ox}) current densities along with calculated film growth (i_{ox}) during passivation of Ni-22 Cr-6 Mo at $+0.2 V_{SCE}$ in 0.1 M NaCl pH 10. Instantaneous DC current densities had their time convoluted in order to put them on the same scale as ICP-MS measurements.

Additional film composition analysis was accomplished for the alkaline experiments is given in Figure 10. The data in Figure 10 indicate that there is very minimal variability in film composition at all times at pH 10, with the exception of some slight Ni-depletion after 3 ks for Ni-Cr-Mo. Ni-Cr-Mo oxide films appear to be slightly more enriched in Cr than in the case of Ni-Cr due to Mo promoting Cr oxidation.^{1,55,62,85–88} Mo is also captured in the oxide at small cation fractions over all times, reaching its maximum overall fraction at the start of experimentation (1.35 at%) and slowly decreasing with time as Mo becomes selectively dissolved.

Oxidation state of the film during passivation according to X-Ray photoelectron spectroscopy.—An example of the XPS spectra deconvolution for Ni-Cr-Mo passivated for 10 ks in 0.1 M NaCl pH 4 is shown in Figure 11. The fitted peaks indicate each observed metallic, hydroxide, and oxide species. Based on the spectra peaks, the hydroxide and oxide species were consistent with Ni(OH)₂, NiO, Cr(OH)₃, Cr₂O₃, MoO₂, and MoO₃ based on the utilized spectral fitting param-

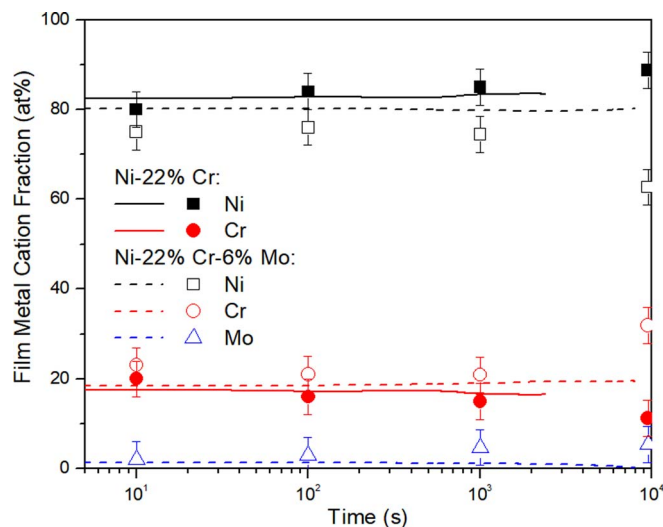


Figure 10. Relative accumulation of metal cations in the passive films during growth until the time of localized corrosion initiation at $+0.2 V_{SCE}$ according to ICP-MS (lines) and XPS (symbols) measurements on Ni-22 Cr and Ni-22 Cr-6 Mo, wt%, in 0.1 M NaCl pH 10.

eters given in Table II.^c Previous literature has additionally identified spinel compounds (e.g. NiCr₂O₄),^{41,45,46,89,90} but these were found to constitute an insignificant fraction (~1%) of the total integrated area, and as such, were excluded from analysis. The integrated peak areas for the aforementioned passive film species are directly compared to each other, and the ICP-MS measurements of film metal cation composition for both alloys passivated at $+0.2 V_{SCE}$ in 0.1 M NaCl adjusted to pH 4 and 10 are given in Figures 7 and 10, respectively.

In an acidic environment, Ni-Cr-Mo films eventually exhibited greater enrichment of Cr resulting in a higher cation fraction of Cr³⁺. This result agrees with the previous observation that Ni-rich films form first, followed by the slower growth of Cr-rich oxides (Figures 5–6).^{41,50} Additionally, the result supports the previous theory⁵² that Mo alloying promotes the oxidation of Cr.⁹¹ There is an apparent difference between the films formed by passivation in an acidic environment (Figure 7) to an alkaline one (Figure 10). Notably, the fraction of Ni²⁺ as measured using XPS peak fitting and ICP-MS analysis remained steady for Ni-Cr films, whereas there was minor enrichment of Cr³⁺ within the film on Ni-Cr-Mo relative to Ni²⁺ throughout the passivation time. For all times, there was a slightly greater fraction of Cr³⁺ within the film on Ni-Cr-Mo than on Ni-Cr after 10 ks (Figures 7 and 10). Finally, the calculated enrichment of Mo⁴⁺ cations was lower for pH 10 (Figure 10) than that observed at pH 4 (Figure 7), due to its likely selective dissolution in the alkaline environment as MoO₄²⁻.

Passive film assessment using neutron reflectometry.—The benefit of these studies was that the in-situ analysis does not involve any air transfer. The reflectivity curves for the two alloys in each solution are given in Figure 12. These data sets were fitted using an algorithm developed by Parratt^{76–79} to produce neutron SLD profiles versus depth (Figure 13). At shallow depths, the SLD corresponded to the electrolyte layer, followed by a gradual increase upon reaching the hydrated gel⁹² at the film surface and then a steep, almost linear increase at greater depths where neutrons probe the oxide layer. Finally, the SLD of the base metal alloys was reached at still greater depths. Annotated on Figure 13 as horizontal lines are the theoretical SLD of several stoichiometric oxides. Based on the figures, the profiles suggest a film rich in Ni-rich oxides. There is no clear layering of stoichiometric oxides within the passive film as a plateau within the pseudo-linear region would be evident, and instead there is a broad,

^cIt should be noted that XPS compound assignments to stoichiometric oxides do not alone prove the existence of stoichiometric oxides because XPS binding energies are dominated by first nearest neighbor interactions and these would not vary for nonstoichiometric species.

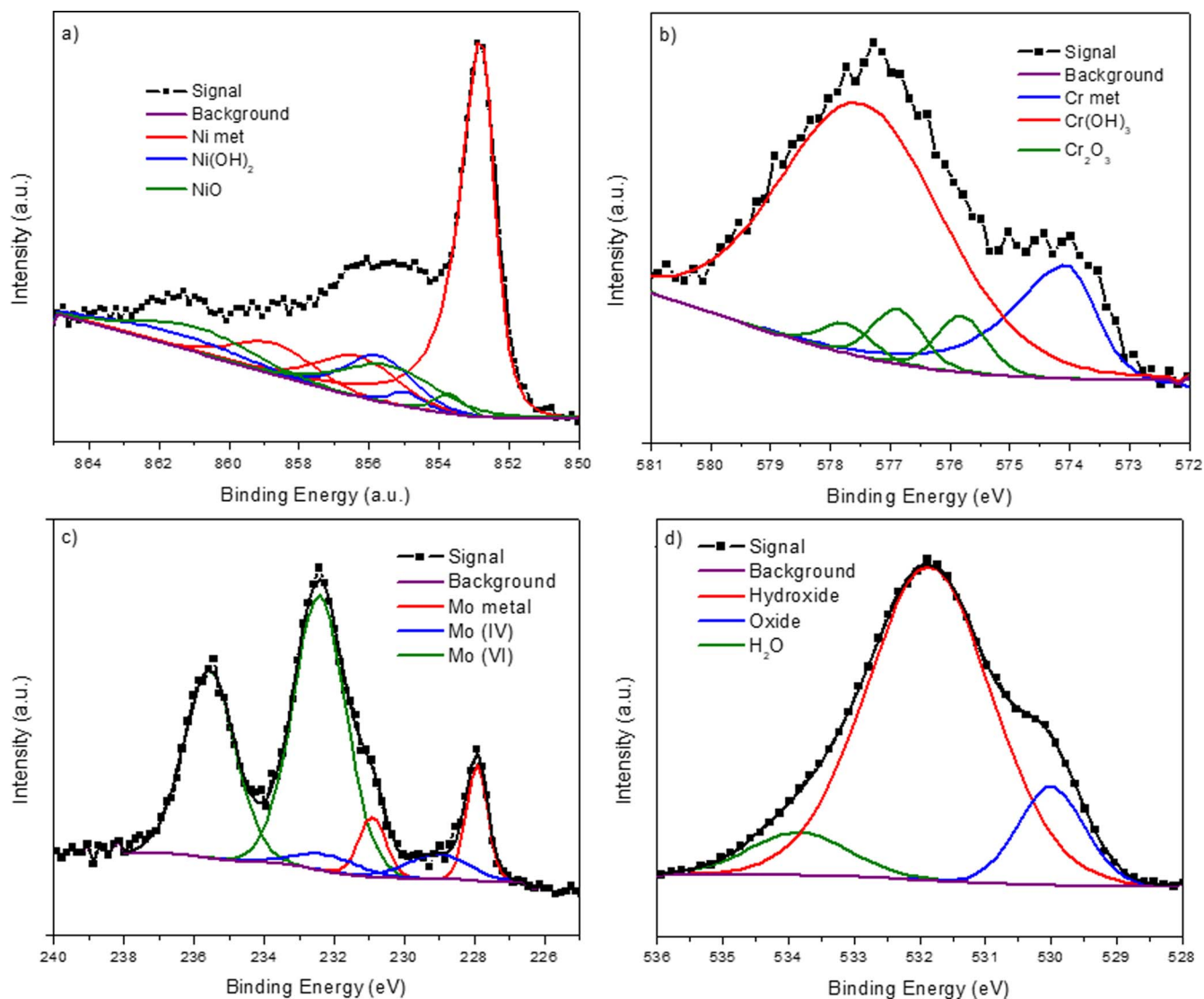


Figure 11. De-convoluted XPS spectra for a) Ni 2p^{3/2}, b) Cr 2p^{3/2}, c) Mo 3d, and d) O 1s bands collected on Ni-22 Cr-6 Mo, wt%, passivated at +0.2 V_{SCE} for 10 ks in 0.1 M NaCl pH 4.

Table II. Spectral fitting parameters used to fit XPS data (Figures 7, 10, and 11) and obtain film composition analysis based on previous literature⁷⁰ where the three most prominent peaks were used. The 2p^{3/2} (Ni and Cr) and 3d (Mo) orbitals were used for analysis.

Compound	Peak B.E. (eV)	FWHM ^a (eV)	%	Compound	Peak B.E. (eV)	FWHM ^a (eV)	%	
Ni	852.6 ^b	0.95	81.2	Cr	574.2	0.90	100	
	856.3	2.70	6.3		Cr(OH) ₃	577.3	2.60	100
	858.7	2.70	12.5			575.7	0.94	40.0
Ni(OH) ₂	854.9	1.16	8.1	Cr ₂ O ₃	576.7	0.94	38.9	
	855.7	2.29	49.3		577.5	0.94	21.1	
	861.5	4.65	42.6	Mo	227.9	0.78	60	
NiO	853.7	1.02	15.4			231.0	0.78	40
	855.4	3.20	47.8		MoO ₂	229.5	2.70	60
	860.9	3.76	36.8		232.6	2.70	40	
				MoO ₃	232.4	1.65	60	
					235.5	1.65	40	

^aFWHM used were for 20 eV pass energy.

^bAsymmetric CasaXPS peak shape = LA(1.1,2.2,10).

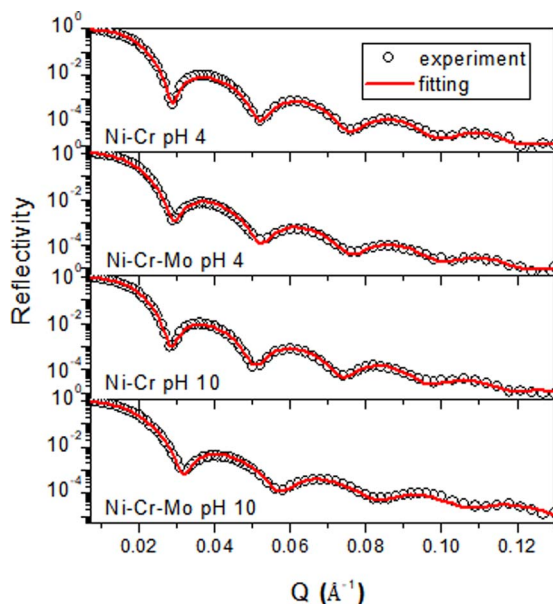


Figure 12. In-situ neutron reflectometry data collected during potentiostatic experiments and the fitted reflectivity curves for deposited Ni-20% Cr and Ni-20% Cr-10% Mo, wt%, films exposed to 0.1 M NaCl pH 4 and pH 10 solution.

continuous increase between the SLD for $\text{Cr}(\text{OH})_3$ and either the peak SLD (for Ni-Cr films) or that of the base metal (for Ni-Cr-Mo films). The simulated SLD profiles produced using GenX software⁷⁹ for either a model non-equilibrium, solute-captured film with varying Cr^{3+} content in NiO (e.g. $\text{Cr}_{1-x}\text{Ni}_x\text{O}_{1.5-x/2}$) or a bilayer oxide composed of varying thickness NiO and Cr_2O_3 layers are provided in Figure 14. Upon comparing Figures 13 and 14, it is evident that the SLD agrees with a single, solute-captured, non-stoichiometric oxide, as shown in Figure 14a. It could be argued that the layered NiO and Cr_2O_3 might agree with experimental data when there is a small l_{ox} for the latter species, but the XPS results (Figures 7, 10, and 11) indicated the oxide was rich with Cr_2O_3 and $\text{Cr}(\text{OH})_3$. The observation that a Cr_2O_3 layer was thin (i.e. less than 1 nm) is therefore non-representative of the observed film composition.

In order to better analyze the composition and thickness of the passive film, the profiles for the unoxidized alloys deposited on SiO_2 and exposed to vacuum, along with H_2O adjacent to a vacuum, were simulated using GenX software and the experimental interfacial roughness and SLD values (Figure 15a).⁷⁹ The SLD for the simulated base metal/vacuum and H_2O /vacuum were then subtracted from the experimental profiles at the first deviation from the alloy SLD, as indicated in Figure 15a, in order to extract the SLD versus depth data for only the passive films. The results, shown in Figure 15b, allow for the estimation of l_{ox} and the Cr^{3+} cation fraction using the width and height of the profile, respectively (Table III). Notably at lower depths, there is a “tail” in the SLD profile which corresponds to a rough, hydrated oxide surface and because of this, only the primary and dominant

peak is considered. Oxide films with an SLD closer to the value of NiO ($8.7 \times 10^{-6} \text{ \AA}^{-2}$) will have a lower % Cr^{3+} compared to those near the value of Cr_2O_3 ($5.1 \times 10^{-6} \text{ \AA}^{-2}$) which would be very Cr rich. A solute-captured rocksalt or corundum film (e.g. $\text{Cr}_{1-x}\text{Ni}_x\text{O}_{1.5-x/2}$ or $\text{Cr}_{2-x}\text{Ni}_x\text{O}_{3-x/2}$) instead of pure, stoichiometric oxides which would have an SLD in-between the latter compounds.^{50d} There is also a decrease in the SLD evident when comparing Ni-Cr to Ni-Cr-Mo films due to the increased enrichment of Cr-rich oxides. Because $\text{Mo}^{4,6+}$ is insignificant compared to Ni^{2+} and Cr^{3+} (Figures 7 and 10), the solute-capture of $\text{Mo}^{4,6+}$ in the oxide would not result in the observed, substantial decrease in the SLD for passivated Ni-Cr-Mo. The effect must be accounted for by increased Cr. For the pH 10 environment, the passive films on the two alloys indicated approximately the same thickness whereas at pH 4, the profile for the Ni-Cr film was significantly broader and, thus, the film was indicated to be thicker than the film on Ni-Cr-Mo (Figure 15b and Table III). This is consistent with the SF-EIS, ICP-MS, and XPS results.

Discussion

Factors governing the chemical identity and composition of passivating oxide.—The thermodynamic favorability of Cr-rich oxides and spinels relative to NiO and $\text{Ni}(\text{OH})_2$ is well known. For instance, $\Delta G_f^{\circ} \text{ NiO} = -212 \frac{\text{kJ}}{\text{mol}}$, $\Delta G_f^{\circ} \text{ Ni}(\text{OH})_2 = -447 \frac{\text{kJ}}{\text{mol}}$, $\Delta G_f^{\circ} \text{ Cr}_2\text{O}_3 = -1,058 \frac{\text{kJ}}{\text{mol}}$, $\Delta G_f^{\circ} \text{ Cr}(\text{OH})_3 = -834 \frac{\text{kJ}}{\text{mol}}$, and $\Delta G_f^{\circ} \text{ NiCr}_2\text{O}_4 = -1,257 \frac{\text{kJ}}{\text{mol}}$.⁹³ Based on both conventional Pourbaix diagrams^{81,94} and chemical stability diagrams,⁹⁵ the expected stoichiometric oxides at +0.2 V_{SCE} are Cr_2O_3 and $\text{Cr}(\text{OH})_3$ in acidic and alkaline environments, while NiO and $\text{Ni}(\text{OH})_2$ are stable at a pH greater than 5.^{83,84}

The results in Figure 7 appear to differ from these predictions. The film measurements suggested the predominance of Ni^{2+} cations. At early oxidation times, rapid oxidation results in passive film cation fractions similar to the bulk metal composition of each alloying element as a result of non-equilibrium solute capture (NSC), i.e. 22 wt% Cr^{3+} becomes frozen into the NiO lattice as non-stoichiometric $\text{Cr}_{1-x}\text{Ni}_x\text{O}_{1.5-x/2}$.⁵⁰ However, gradual enrichment of Cr^{3+} results in the behavior shown in Figures 7 and 10. Additionally, the SLD profiles in Figures 13 and 14 suggest the existence of solute-captured films as no distinct layers are observed. The results indicate a very different picture of aqueous electrochemical passivation than has been previously reported.^{1,16,25,35,40,96-100} Ni and Cr are oxidized at equivalent rates during the early stages of passivation in acidic and alkaline chloride solutions according to the ICP-MS (Figures 5–10) and XPS (Figures 7 and 10) results. NiO formation might be energetically favored if the rocksalt structure is more compatible with the fcc Ni-Cr lattice. This factor is not taken into consideration in conventional E-pH diagrams.

Passivation in the alkaline environment (Figure 10) suggests that the Ni^{2+} cations in the film remain in the passive film at all times and no preferential ejection occurs, enabling Cr^{3+} enrichment. Instead, film thickening continues with notably slower preferential enrichment of the more thermodynamically stable, Cr-rich species. Similar stability of Ni^{2+} -rich oxides in an alkaline environment was observed in previous literature.⁹⁹ The concentrations of Mo^{4+} and Mo^{6+} cations, as governed initially by NSC, both increased in the film with passivation time, with the latter having greater XPS peak areas and thus a greater film concentration (noted in Figure 11), albeit both concentrations were low compared to those of Ni^{2+} and Cr^{3+} . It is possible that $\text{Mo}^{4,6+}$ substitutes for Cr^{3+} in the films, as will be discussed later.

The interplay between kinetics and thermodynamic factors apparently results in the nucleation and growth of NiO/ $\text{Ni}(\text{OH})_2$ along with $\text{Cr}_2\text{O}_3/\text{Cr}(\text{OH})_3$.^{99,100} When surface energy is factored into oxide stability, the Ni/NiO rocksalt epitaxial relationship with an FCC, Ni-based

Table III. Fraction of Cr cations in the film and final thickness measured in the subtracted oxidation SLD profiles for Ni-20 Cr and Ni-20 Cr-10 Mo, at%, passivated up to +0.2 V_{SCE} in 0.1 M NaCl at pH 4 and 10 as shown in Figures 13 and 15.

Environment	Alloy	SLD max $\times 10^6$ (\AA^{-2})	Cr^{3+} in NiO (at%)	l_{ox} (nm)
Cl pH 4	NiCr	7.8	37	7.4
	NiCrMo	6.8	68	5.0
Cl pH 10	NiCr	7.9	32	5.5
	NiCrMo	7.2	56	4.4

^dAn alternative interpretation is that islands of phase distinct, high purity Cr_2O_3 and NiO form at length scales smaller than the neutron beam such that an average signal is obtained. This nanoscale heterogeneous surface has not yet been observed experimentally^{41,44,50,100} and would be prone to localized corrosion at the Cr-depleted surface areas.

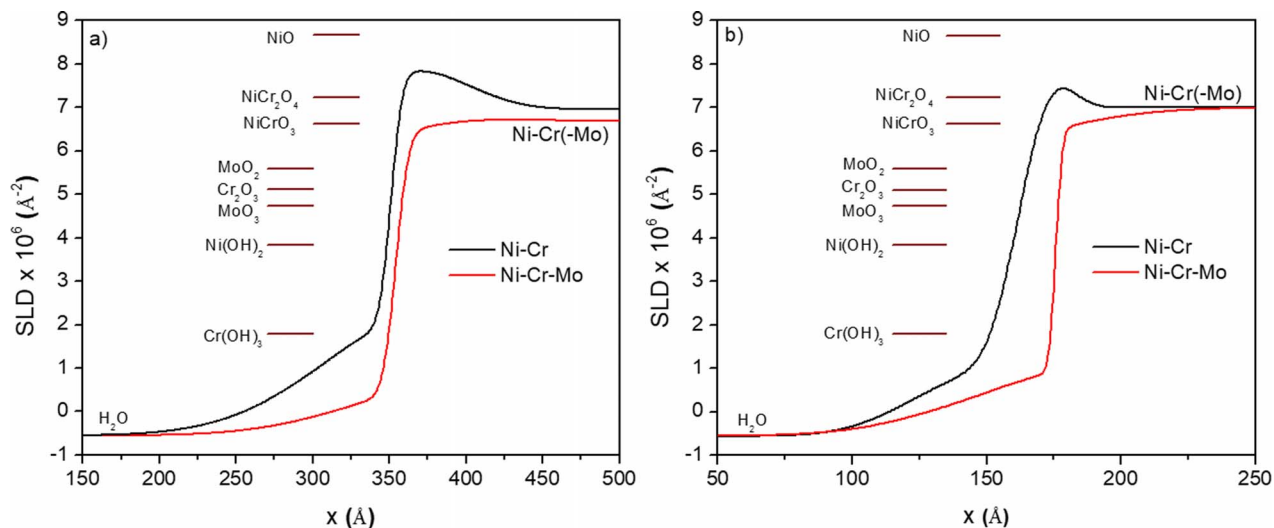


Figure 13. SLD profiles obtained for deposited Ni-20% Cr and Ni-20% Cr-10% Mo, wt%, films passivated up to $+0.2 V_{\text{SCE}}$ in a) 0.1 M NaCl pH 4 and b) 0.1 M NaCl pH 10 solutions with the theoretical SLD for various possible compounds shown to indicate their presence and distribution through the films.

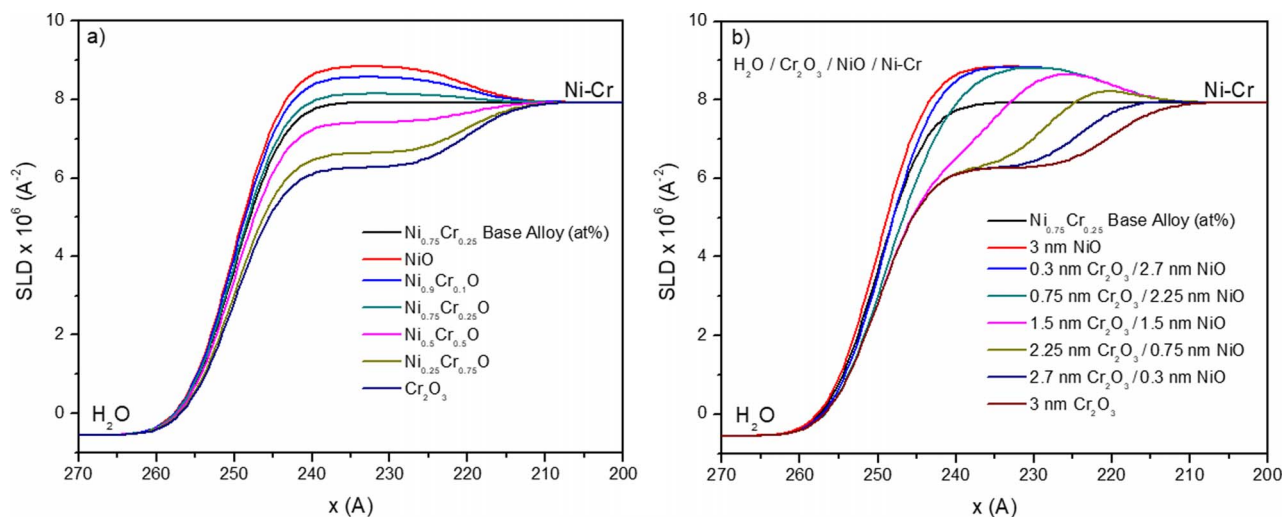


Figure 14. Simulated SLD profiles for a) a solute-captured rocksalt-structured oxide, $\text{Ni}_{1-x}\text{Cr}_x\text{O}_3$, containing varying % Cr^{3+} and b) a bilayer oxide comprised of Cr_2O_3 and NiO with varying thicknesses of each conformal layer. An interfacial roughness of 5 \AA was used to replicate the experimental parameters.

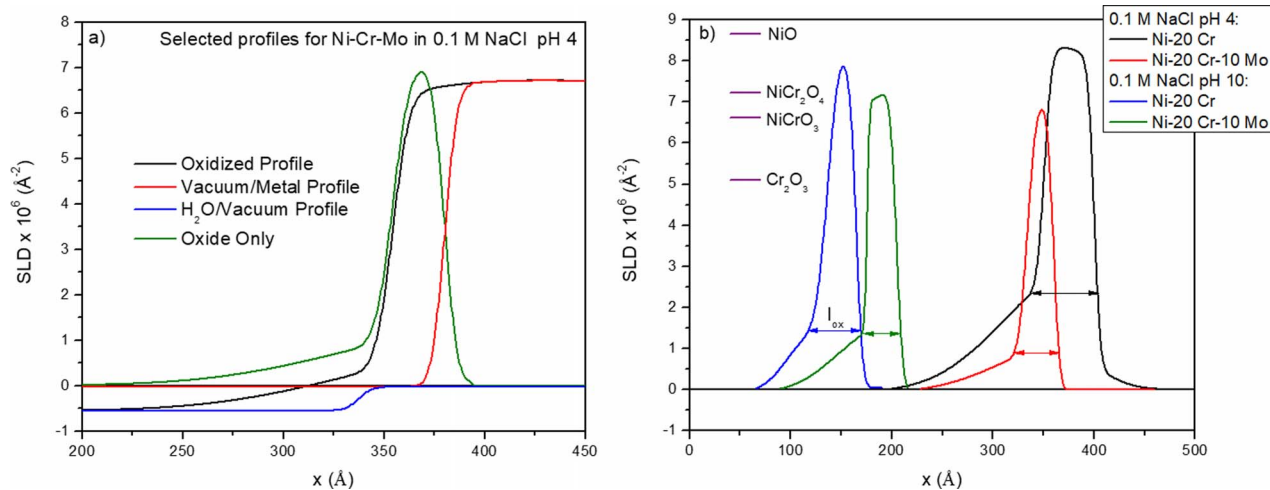


Figure 15. Analysis of the NR profiles given in Figure 13 where a) SLD profiles for the base metal on the Si substrate and for the electrolyte layer exposed to vacuum were simulated and subtracted from the overall SLD profile in order to obtain that of just the passive film for Ni-Cr-Mo in 0.1 M NaCl pH 4 and b) the oxide-only profiles for each alloy and environment combination are provided. The peak SLD correlates to the Ni^{2+} cation fraction (Figure 14a) and the approximate l_{ox} is indicated by the peak width.

substrate may favor NiO formation and subsequently hydrated, overlying Ni(OH)₂.^{25,101–103} Later during passivation, enrichment was said to be driven by thermodynamic factors.^{103,104} However, early stages of oxidation appear to favor Cr_{1-x}Ni_xO_{1.5-x/2} instead of stoichiometric oxides. Preferential dissolution of Ni²⁺ in chloride environments enables further enrichment of Cr³⁺ in the film and eventually leads to dominance by Cr_{2-x}Ni_xO_{3-1/2x}. Following 8+ hrs of passivation in harsh chloride electrolytes, this enrichment has been previously shown to result in Cr-rich species dominating the passive film for similar commercial Ni alloys.^{1,16,40,105,106} Notably, Ni-20 wt% Cr passivated in 1 M NaOH and 0.5 M H₂SO₄ exhibited a film richer in Cr³⁺ in the case of the latter environment and became increasingly enriched with time.⁹⁹ At these longer times, significant enrichment of solute Cr³⁺ cations can result in the formation of non-stoichiometric corundum with a chemical composition of Cr_{2-x}Ni_xO_{3-y}. This classically Cr³⁺-rich film can still contain significant amounts of Ni²⁺ cations until longer times at which point annealing would produce stoichiometric films not representative of NSC.⁵⁰ The oxides evidently first form according to the principles of NSC kinetics until a steady-state has been reached and thermodynamics controls the film structure and composition.²⁵ A previous LEED study of Ni-Cr oxidation demonstrated that short term oxidation resulted in Cr_{1-x}Ni_xO_{1.5-x/2} while long term oxidation formed a spinel.¹⁰⁰

Effects of Mo on passivation.—In previous work, the existence of Mo-oxides within passive films was proposed with some explanation of the quantity and/or location.¹⁰⁷ Moreover, the cation molecular identity was attributed to stoichiometric MoO₂ and MoO₃.^{81,108–110} The presence of Mo alloying additions also resulted in the increased enrichment of Cr³⁺ within the passive film.^{1,91} This phenomenon is evident in Figures 7 and 10, where the fraction of Cr³⁺ tends to be higher, especially after long passivation times. Fundamental density-functional theory (DFT) models have recently demonstrated that Mo promotes the adsorption of O on Ni-Cr surfaces.⁹¹ In particular, the theorized synergistic oxidation of Cr in the presence of Mo was shown to result from the favorable adsorption energy compared to surface sites containing Ni. In this (Figures 7 and 10 and Table III) and previous passivation studies,^{1,61,62,64} similar behavior has been observed where Ni-Cr-Mo alloys exhibited greater fractions of Cr³⁺ species in their films. Other recent DFT studies have demonstrated the increased favorability of corundum upon alloying with Mo, where the driving force for nucleation decreases by 0.64 eV per Mo atom in the oxide formula unit cell.⁴¹ The impact of Mo on encouraging Cr passivation is only one of the several proposed theories regarding film growth and stability.⁵²

The observed influence of Mo on oxidation processes has also been attributed to the element acting as a dopant with very high concentrations (at% rather than ppm) and modifying the electronic properties of the ternary alloy. The addition of small concentrations of Mo⁶⁺ in the passive film will result in the formation of substitutional defects (i.e. Mo_{Ni}⁴⁺ and Mo_{Cr}³⁺) following NSC.^{41,50,111} The SVM suggests this phenomena will result in improvements in the film's electrochemical stability following the annihilation of metal cation vacancies (e.g. V_{Ni}^{''} and V_{Cr}^{'''}), which are theorized to be major contributors to the initiation of localized corrosion.^{51,111} This is posited to occur by the interaction between the positively-charged substituted Mo site and negatively-charged metal cation vacancies, forming less mobile, neutral defects. The diffusion of these defects is not accelerated by the electric field and, as such, will not contribute toward film growth and/or breakdown reactions.^{51,54,112}

Conclusions

The passivation and dissolution of Ni-22 Cr and Ni-22-6 Mo (wt%), were investigated during in-operando potentiostatic passivation using electrochemical ICP-MS and SF-EIS in both acidic and alkaline NaCl environments, coupled with in-situ NR and ex-situ XPS conducted during and following film growth. The combination of the techniques

utilized enabled determination of i_{ox} distinctly from i_{EC} with high temporal resolution. Contrary to some previous work which suggested rapid Cr₂O₃ formation in a chloride-free environment, it was determined that both Ni and Cr-rich films form early during the passivation process, indicating the combined influence of thermodynamic and kinetic factors. Surface films produced during anodic polarization at +0.2 V_{SCE} were consistent with non-stoichiometric solid solution rocksalt and corundum oxide structures, likely containing solute captured Ni²⁺, Cr³⁺, and Mo^{+4,6} cations. Limited layering was observed during oxide formation, with the films instead being Ni-rich at the film/electrolyte and Cr-rich at the metal/film interfaces. Oxides compositions were initially governed by non-equilibrium solute capture. At long times, kinetic factors enabled enrichment whereas thermodynamics determined the longer-term passive film behavior. The electrochemical stability of Cr³⁺ cations in the passive films increased with alloying of Mo in the base metal, noted by the dissolution currents for the Ni-Cr-Mo alloy in each environment. Surface films produced during anodic polarization in the alkaline environment were found to be enriched in Ni²⁺ cations because of the increased stability of NiO and Ni(OH)₂.

Acknowledgments

Special Thanks to Matthew Taylor at the University of Wisconsin for producing the alloys used for this study. KLC, PR, and JRS acknowledge support from ONR MURI "Understanding Atomic Scale Structure in Four Dimensions to Design and Control Corrosion Resistant Alloys" on grant #N00014-14-1-0675. Hung Ha was supported by FST 51100.50.11 work package and CNBC 62400.01.02 project. Useful discussion with Zin Tun and Helmut Fritzsche at CNBC is also acknowledged.

Appendix A – ICP-MS Data Analysis Methods

The element-specific current density contributions for cation species, Mⁿ⁺, released into solution and not retained in the oxide as determined by the ICP measurements, i_{ICP}^M , were computed and summed to obtain i_{ICP} , the total current density for dissolution and cation ejection reactions:

$$C_M = k (I_x - I_x^0) \quad [A1]$$

$$i_M(t) = \frac{nFk_f e [I_x(t) - I_x^0]}{M_M} \quad [A2]$$

$$i_{ICP} = \sum i_{ICP}^M \quad [A3]$$

where I_x is measured emission intensity of a given element, M , I_x^0 is background intensity, k is a proportionality constant, C is concentration of element M in the electrolyte stream, F is Faraday's constant, f_e is electrolyte flow rate, and M_M is molar mass of element M . The total ICP current was then subtracted from the total electrochemically measured DC current density, i_{EC} , associated with the total metal oxidation and dissolution in order to compute the total oxide formation current density, i_{ox} :

$$i_{ox}^{ICP} = i_{EC} - i_{ICP} \quad [A4]$$

In order to evaluate the contribution of a specific element, M , toward passivation rather than direct cation ejection or film dissolution, the expected, element-specific dissolution current density based on congruent alloy dissolution where E_{app} is well above the Nernst E_r and E_{pp} ¹¹³ for each element was computed and the oxidation contribution was similarly obtained using i_{ICP}^M :

$$i_{cong\ diss}^M = (at\% M) i_{EC} \quad [A5]$$

$$i_{ox}^M = i_{cong\ diss}^M - i_{ICP}^M \quad [A6]$$

From the total oxide formation current density (Eq. A4), the overall film thickness, l_{ox} , can be obtained:

$$l_{ox}(t) = \frac{M_{ox}}{nF\rho_{ox}} q_{ox}(t) = \frac{M_{ox}}{nF\rho_{ox}} \int_0^t i_{ox}(t) dt \quad [A7]$$

where M_{ox} is the overall oxide molar mass, n is the metal cation valency, and ρ_{ox} is the overall oxide density, which have been estimated previously.²⁵ The film's overall atomic

composition, C_M , can then be calculated from a combination of electrochemistry and ICP-MS using the following expressions²:

$$N_M(t) = \frac{N_A}{nF} q_{ox}^M(t) = \frac{N_A}{nF} \int_0^t i_{ox}^M(t) dt \quad [A8]$$

$$C_M(t) = \frac{N_M(t)}{N_{Ni}(t) + N_{Cr}(t) + N_{Mo}(t)} \quad [A9]$$

where N_M is the atomic area density of element M on the alloy surface and N_A is Avogadro's number.

Appendix B – SF-EIS Data Analysis Methods

The impedance results were analyzed using the following expressions:^{114,115}

$$Q_{CPE} = \frac{(\varepsilon\varepsilon_0)^\alpha}{g_{ox}\rho_\delta^{1-\alpha}} \quad [B1]$$

$$-Z'' = \frac{\sin\left(\frac{\alpha\pi}{2}\right)}{Q_{CPE}(2\pi f)^\alpha} \quad [B2]$$

where g is given as:¹¹⁴

$$g = 1 + 2.88(1 - \alpha)^{2.375} \quad [B3]$$

The combination of Eqs². B1–B3 yields:

$$I_{ox}(t) = \frac{-(2\pi\varepsilon\varepsilon_0 f)^\alpha Z''(t)}{g\rho_\delta^{1-\alpha} \sin\left(\frac{\alpha\pi}{2}\right)} \quad [B4]$$

where Q_{CPE} is the constant phase element parameter, α is the constant phase element exponent, ε is the film dielectric constant assumed to be approximately 30 as the composite average for passive films grown on Ni-Cr-based alloys,³⁷ ε_0 is the vacuum permittivity of free space, ρ_δ is the boundary interfacial resistivity approximated to be 450 Ω -cm based on the value previously used for stainless steels,¹¹⁶ f is the frequency used for impedance measurements, and $Z''(t)$ is the imaginary component of SF-EIS dominated by oxide capacitance at a designated frequency that increases in magnitude as a passive oxide film thickens and is negative for capacitive films.

The oxidation current density was calculated as the derivative of oxide thickness measured by SF-EIS and using previously computed constants for a film consisting of a mixture of Ni and Cr-rich oxides and hydroxides:²⁵

$$i_{ox}^{SF}(t) = \frac{nF\rho_{ox}}{M_{ox}} \frac{dI_{ox}}{dt} \quad [B5]$$

List of Symbols

C_M	Concentration of element M
E_{app}	Applied potential
E_{pp}	Critical passivation potential
E_r	Nernst potential
f	Applied frequency
f_e	Electrolyte flow rate
F	Faraday's constant
g	SF-EIS interpolation function
I_h	Measured emission intensity of a specific element
I_b^o	Background emission intensity
i_{cong}^M	Estimated congruent dissolution current for a specific element M
i_{EC}	Total anodic current density
i_{ICP}	Total measured dissolution current density
i_{ICP}^M	Dissolution current density for a specific element M
i_{ox}^{SF}	Total oxide formation current density as determined using SF-EIS
i_{ox}^{ICP}	Total oxide formation current density as determined using i_{EC} and i_{EC}^M
i_{ox}^M	Oxidation current density for a specific element M
k	Proportionality constant
l_{ox}	Passive film thickness
M_M	Molar mass of a specific element M
M_{ox}	Molar mass of oxide film
n	Cation valency
N_A	Avogadro's number
N_M	Atomic surface area density of a specific element M
q	Electron elementary charge
Q_{CPE}	Constant phase element parameter
Q	Scattering vector

²It is recognized that this computed composition does not account for potential layering.

R_{ox}	Oxide Resistance
t	Time
Z''	Imaginary impedance component

Greek

α	Constant phase element exponent
ΔG_f^o	Standard Gibb's formation energy
ε	Dielectric constant
ε_0	Vacuum permittivity of free space
λ	Neutron beam wavelength
ρ_{ox}	Oxide density
ρ_δ	Boundary interfacial resistivity
θ	Neutron beam incident angle

ORCID

Katie Lutton Cwalina  <https://orcid.org/0000-0002-5356-4470>

Hung M. Ha  <https://orcid.org/0000-0002-1461-8835>

John R. Scully  <https://orcid.org/0000-0001-5353-766X>

References

1. A. C. Lloyd, J. J. Noël, S. McIntyre, and D. W. Shoesmith, *Electrochim. Acta*, **49**, 3015 (2004).
2. D. D. MacDonald and A. Sun, *Electrochim. Acta*, **51**, 1767 (2006).
3. P. Jakupi, D. Zagidulin, J. J. Noël, and D. W. Shoesmith, *Electrochim. Acta*, **56**, 6251 (2011).
4. R. D. Willenbruch, C. R. Clayton, M. Oversluis, D. Kim, and Y. Lu, *Corros. Sci.*, **31**, 179 (1990).
5. D. Zagidulin, X. Zhang, J. Zhou, J. J. Noël, and D. W. Shoesmith, *Surf. Interface Anal.*, **45**, 1014 (2013).
6. E. De Vito and P. Marcus, *Surf. Interface Anal.*, **19**, 403 (1992).
7. N. Sato and K. Kudo, *Electrochim. Acta*, **19**, 461 (1974).
8. N. Sato and K. Kudo, *Electrochim. Acta*, **16**, 447 (1971).
9. M. Seo, R. Saito, and N. Sato, *J. Electrochem. Soc.*, **127**, 1909 (1980).
10. C. Lukac, J. B. Lumsden, S. Smialowska, and R. W. Staehle, *J. Electrochem. Soc.*, **122**, 1571 (1975).
11. Z. Tun, J. J. Noel, and D. W. Shoesmith, *J. Electrochem. Soc.*, **146**, 988 (1999).
12. H. Ha, H. Fritzsche, G. Burton, and J. Ulaganathan, *J. Electrochem. Soc.*, **164**, C699 (2017).
13. H. Ha, H. Fritzsche, G. Burton, and J. Ulaganathan, *J. Electrochem. Soc.*, **164**, C258 (2017).
14. D. G. Wiesler and C. F. Majkrzak, *Phys. B Condens. Matter*, **198**, 181 (1994).
15. V. Maurice, H. Peng, L. H. Klein, A. Seyeux, S. Zanna, and P. Marcus, *Faraday Discuss.*, **180**, 151 (2015).
16. A. C. Lloyd, J. J. Noël, N. S. McIntyre, and D. W. Shoesmith, *JOM*, **57**, 31 (2005).
17. G. T. Burstein and A. J. Davenport, *J. Electrochem. Soc.*, **136**, 936 (1989).
18. A. J. Davenport and G. T. Burstein, *J. Electrochem. Soc.*, **137**, 1496 (1990).
19. A. J. Davenport and B. K. Lee, *Electrochem. Soc. Proc.*, **13**, 187 (2002).
20. N. Sato and M. Cohen, *J. Electrochem. Soc.*, **111**, 512 (1964).
21. N. Sato and M. Cohen, *J. Electrochem. Soc.*, **111**, 519 (1964).
22. R. Goetz, B. MacDougall, and M. J. Graham, *Electrochim. Acta*, **31**, 1299 (1986).
23. K. Ogle and S. Weber, *J. Electrochem. Soc.*, **147**, 1770 (2000).
24. D. Hamm, K. Ogle, C. O. Olsson, S. Weber, and D. Landolt, *Corros. Sci.*, **44**, 1443 (2002).
25. K. Lutton, K. Gusieva, N. Ott, N. Birbilis, and J. R. Scully, *Electrochem. Commun.*, **80**, 44 (2017).
26. S. O. Klemm, J.-C. Schauer, B. Schuhmacher, and A. W. Hassel, *Electrochim. Acta*, **56**, 4315 (2011).
27. J. Klemm, S. Klemm, M. Duarte, L. Rossrucker, K. J. J. Mayrhofer, and F. U. Renner, *Corros. Sci.*, **89**, 59 (2014).
28. N. Ott, A. Beni, A. Ulrich, C. Ludwig, and P. Schmutz, *Talanta*, **120**, 230 (2014).
29. J. D. Henderson, X. Li, D. W. Shoesmith, J. J. Noël, and K. Ogle, *Corros. Sci.*, **147**, 32 (2019).
30. M. J. Duarte, J. Klemm, S. O. Klemm, K. J. J. Mayrhofer, M. Stratmann, S. Borodin, A. H. Romero, M. Madinehi, D. Crespo J. Serrano, S. S. A. Gerstl, P. P. Choi, D. Raabe, and F. U. Renner, *Science*, (80-.), **341**, 372 (2013).
31. F. Bocher, R. Huang, and J. R. Scully, *Corrosion*, **66**, 1 (2010).
32. X. Zhang and D. W. Shoesmith, *Corros. Sci.*, **76**, 424 (2013).
33. M. A. Rodríguez, R. M. Carranza, and R. B. Rebak, *J. Electrochem. Soc.*, **157**, C1 (2010).
34. J. R. Hayes, J. J. Gray, A. W. Szmodis, and C. A. Orme, *Corrosion*, **62**, 491 (2006).
35. J. J. Gray, J. R. Hayes, G. E. Gdowski, B. E. Viani, and C. A. Orme, *J. Electrochem. Soc.*, **153**, B61 (2006).
36. D. G. Enos and C. R. Bryan, *Corrosion*, **71**, 758 (2015).
37. D. D. Macdonald, A. Sun, N. Priyantha, and P. Jayaweera, *J. Electroanal. Chem.*, **572**, 421 (2004).
38. P. Jakupi, J. J. Noel, and D. W. Shoesmith, *Corros. Sci.*, **53**, 3122 (2011).

39. N. Priyantha, P. Jayaweera, D. D. Macdonald, and A. Sun, *J. Electroanal. Chem.*, **572**, 409 (2004).
40. X. Zhang, D. Zagidulin, and D. W. Shoesmith, *Electrochim. Acta*, **89**, 814 (2013).
41. X. Yu, A. Gulec, C. M. Andolina, E. J. Zeitchick, K. Gusieva, J. C. Yang, J. R. Scully, J. H. Perepezko, and L. D. Marks, *Corrosion*, **74**, 939 (2018).
42. L. Kjellqvist, M. Selleby, and B. Sundman, *Calphad Comput. Coupling Phase Diagrams Thermochem.*, **32**, 577 (2008).
43. A. Y. W. Lin, A. Müller, X. Yu, A. M. Minor, and L. D. Marks, *Ultramicroscopy*, (2019).
44. X. Yu, A. Gulec, K. Lutton Cwalina, J. Scully, and L. Marks, *Corrosion*, (2019).
45. L. Luo, L. Zou, D. K. Schreiber, D. R. Baer, S. M. Bruemmer, G. Zhou, and C. Wang, *Scr. Mater.*, **114**, 129 (2016).
46. L. Luo, L. Zhou, D. K. Schreiber, M. J. Olszta, D. R. Baer, S. M. Bruemmer, G. Zhou, and C. Wang, *Chem. Commun.*, **52**, 3300 (2016).
47. B. G. Pound and C. H. Becker, *J. Electrochem. Soc.*, **138**, 696 (1991).
48. X. Zhang and D. W. Shoesmith, *Corros. Sci.*, **76**, 424 (2013).
49. B. Kobe, M. Badley, J. D. Henderson, S. Anderson, M. C. Biesinger, and D. Shoesmith, *Surf. Interface Anal.*, **49**, 1345 (2017).
50. X. Yu, A. Gulec, Q. Sherman, K. Lutton Cwalina, J. R. Scully, J. H. Perepezko, P. W. Voorhees, and L. D. Marks, *Phys. Rev. Lett.*, **121**, 145701 (2018).
51. M. Urquidi and D. D. Macdonald, *J. Electrochem. Soc.*, **132**, 555 (1985).
52. K. Lutton Cwalina, C. R. Demarest, A. Y. Gerard, and J. R. Scully, *Curr. Opin. Solid State Mater. Sci.*, (2019).
53. E. McCafferty, *Corros. Sci.*, **42**, 1993 (2000).
54. M. Urquidi-Macdonald and D. D. Macdonald, *J. Electrochem. Soc.*, **136**, 961 (1989).
55. P. I. Marshall and G. T. Burstein, *Corros. Sci.*, **24**, 463 (1984).
56. R. B. Rebak, in *Materials Science and Technology*, p. 71, Wiley-VCH Verlag GmbH & Co. KGaA, Weinheim, Germany (2013).
57. I. Olefjord, B. Brox, and U. Jelvestam, *J. Electrochem. Soc.*, **132**, 2854 (1985).
58. N. Ebrahimi, thesis, The University of Western Ontario (2015).
59. M. Bojinov, G. Fabricius, T. Laitinen, K. Mäkelä, T. Saario, and G. Sundholm, *J. Electroanal. Chem.*, **504**, 29 (2001).
60. L. F. Lin, C. Y. Chao, and D. D. Macdonald, *J. Electrochem. Soc.*, **128**, 1194 (1981).
61. C. R. Clayton and Y. C. Lu, *J. Electrochem. Soc.*, **133**, 2465 (1986).
62. K. Sugimoto and Y. Sawada, *Corrosion*, **32**, 347 (1976).
63. P. Jakupi, F. Wang, J. J. Noël, and D. W. Shoesmith, *Corros. Sci.*, **53**, 1670 (2011).
64. R. S. Lillard, M. P. Jurinski, and J. R. Scully, *Corrosion*, **50**, 251 (1994).
65. K. Matsumoto, S. Kim, J. Wen, and I. Hirabayashi, *IEEE Trans. Appl. Supercond.*, **9**, 1539 (1999).
66. K. Gusieva, K. Lutton Cwalina, W. H. Blades, G. Ramalingam, J. H. Perepezko, P. Reinke, and J. R. Scully, *J. Phys. Chem. C*, **122**, 19499 (2018).
67. N. Cabrera and N. F. Mott, *Reports Prog. Phys.*, **12**, 163 (1949).
68. K. F. Quiambao, S. J. McDonnell, D. K. Schreiber, A. Y. Gerard, K. M. Freedy, P. Lu, J. E. Saal, G. S. Frankel, and J. R. Scully, *Acta Mater.*, **164**, 362 (2019).
69. N. Sato, *J. Electrochem. Soc.*, **129**, 255 (1982).
70. M. C. Biesinger, B. P. Payne, A. P. Grosvenor, L. W. M. Lau, A. R. Gerson, and R. St. C. Smart, *Appl. Surf. Sci.*, **257**, 2717 (2011).
71. F. Werfel and E. Minni, *J. Phys. C Solid State Phys.*, **16**, 6091 (1983).
72. J. F. Moulder, W. F. Stickle, P. E. Sobol, and K. D. Bomben, 261 (1992).
73. M. C. Biesinger, B. P. Payne, L. W. M. Lau, A. Gerson, and R. St. C. Smart, *Surf. Interface Anal.*, **41**, 324 (2009).
74. M. C. Biesinger, B. P. Payne, B. R. Hart, A. P. Grosvenor, N. S. McIntyre, L. W. M. Lau, and R. St. C. Smart, *J. Phys. Conf. Ser.*, **100**, 012025 (2008).
75. J. Baltusaitis, B. Mendoza-Sanchez, V. Fernandez, R. Veenstra, N. Dukstiene, A. Roberts, and N. Fairley, *Appl. Surf. Sci.*, **326**, 151 (2015).
76. H. Fritzsche, F. Klose, C. Rehm, Z. Tun, M. Wolff, and B. Hjörvarsson, in *Neutron Scattering and Other Nuclear Techniques for Hydrogen in Materials*, p. 115, Springer, Cham (2016).
77. J. Penfold and R. K. Thomas, *J. Phys. Condens. Matter*, **2**, 1369 (1990).
78. L. G. Parratt, *Phys. Rev.*, **95**, 359 (1954).
79. M. Björck and G. Andersson, *J. Appl. Crystallogr.*, **40**, 1174 (2007).
80. R. B. Rebak and P. Crook, in *American Society of Mechanical Engineers Pressure Vessels and Piping Division Conference*, p. 1 (2004).
81. M. Pourbaix, *Atlas of electrochemical equilibria in aqueous solutions*, National Association of Corrosion Engineers, (1974).
82. V. Shkirskiy, P. Maciel, J. Deconinck, and K. Ogle, *J. Electrochem. Soc.*, **163**, C37 (2016).
83. L.-F. Huang, M. J. Hutchison, R. J. Santucci, J. R. Scully, and J. M. Rondinelli, *J. Phys. Chem. C*, **121**, 9782 (2017).
84. L.-F. Huang and J. Rondinelli, *Bull. Am. Phys. Soc.* (2018).
85. K. Sugimoto and Y. Sawada, *Corros. Sci.*, **17**, 425 (1977).
86. E. A. Lizlovs and A. P. Bond, *J. Electrochem. Soc.*, **118**, 22 (1971).
87. I. Olefjord, *Mater. Sci. Eng.*, **42**, 161 (1980).
88. A. Tomio, M. Sagara, T. Doi, H. Amaya, N. Otsuka, and T. Kudo, *Corros. Sci.*, **98**, 391 (2015).
89. G. R. Baran, *J. Dent. Res.*, **63**, 1332 (1984).
90. Y. Unutulmazsoy, R. Merkle, J. Mannhart, and J. Maier, *Solid State Ionics*, **309**, 110 (2017).
91. A. J. Samin and C. D. Taylor, *Corros. Sci.*, **134**, 103 (2018).
92. M. P. Ryan, R. C. Newman, and G. E. Thompson, *J. Electrochem. Soc.*, **141**, L164 (1994).
93. J. G. Speight and N. A. Lange, *Lange's handbook of chemistry*, 17th ed., McGraw-Hill Education, New York, (2017).
94. P. Lu, J. E. Saal, G. B. Olson, T. Li, Orion J. Swanson, G. S. Frankel, A. Y. Gerard, K. F. Quiambao, and J. R. Scully, *Scr. Mater.*, **153**, 19 (2018).
95. R. J. Santucci, M. E. McMahon, and J. R. Scully, *npj Mater. Degrad.*, **2**, 1 (2018).
96. R. B. Rebak and J. H. Payer, in *11th International High Level Radioactive Waste Management Conference*, p. 1 (2006).
97. M. A. Rodríguez and R. M. Carranza, *J. Electrochem. Soc.*, **158**, C221 (2011).
98. B. A. Kehler, G. O. Ilevbare, and J. R. Scully, *Passiv. Localized Corros. an Int. Symp. Honor Profr. Norio Sato*, **99**, 644 (1999).
99. T. Jabs, P. Borthen, and H. H. Strehblow, *J. Electrochem. Soc.*, **144**, 1231 (1997).
100. A. Takei and K. Nii, *Trans. Japan Inst. Met.*, **17**, 211 (1976).
101. H. G. Lee, Y. M. Lee, H. S. Shin, C. H. Jung, and G. W. Hong, *Met. Mater.*, **6**, 565 (2000).
102. N. Kitakatsu, V. Maurice, C. Hinnen, and P. Marcus, *Surf. Sci.*, **407**, 36 (1998).
103. L.-F. Huang, H. M. Ha, K. Lutton Cwalina, J. R. Scully, and J. M. Rondinelli, Submitted to *J. Phys. Chem. C* (2019).
104. R. Kirchheim, B. Heine, S. Hofmann, and H. Hofsäss, *Corros. Sci.*, **31**, 573 (1990).
105. A. C. Lloyd, D. W. Shoesmith, N. S. McIntyre, and J. J. Noël, *J. Electrochem. Soc.*, **150**, B120 (2003).
106. N. Ebrahimi, M. C. Biesinger, D. W. Shoesmith, and J. J. Noël, *Surf. Interface Anal.*, **49**, 1359 (2017).
107. J. R. Scully, *Faraday Discuss. Faraday Discuss.*, **180**, 577 (2015).
108. I. A. Okonkwo, J. Doff, A. Baron-Wiechec, G. Jones, E. V. Koroleva, P. Skeldon, and G. E. Thompson, *Thin Solid Films*, **520**, 6318 (2012).
109. W. Yang, R. C. Ni, H. Z. Hua, and A. Pourbaix, *Corros. Sci.*, **24**, 691 (1984).
110. P. A. Spevack and N. S. McIntyre, *J. Phys. Chem.*, **97**, 11020 (1993).
111. M. J. Hutchison and J. R. Scully, *J. Electrochem. Soc.*, **165**, C689 (2018).
112. D. D. Macdonald, *J. Electrochem. Soc.*, **139**, 3434 (1992).
113. J. R. Scully and K. Lutton, *Encycl. Interfacial Chem. Surf. Sci. Electrochem.* (2018).
114. B. Hirschorn, M. E. Orazem, B. Tribollet, V. Vivier, I. Frateur, and M. Musiani, *J. Electrochem. Soc.*, **157**, C452 (2010).
115. B. Hirschorn, M. E. Orazem, B. Tribollet, V. Vivier, I. Frateur, and M. Musiani, *Electrochim. Acta*, **55**, 6218 (2010).
116. Y.-M. Chen, N. G. Rudawski, E. Lambers, and M. E. Orazem, *J. Electrochem. Soc.*, **164**, C563 (2017).